Dissertation
submitted to the
Combined Faculty of Natural Sciences and Mathematics
of the Ruperto Carola University Heidelberg, Germany
for the degree of
Doctor of Natural Sciences

Presented by

M.D. Takehito Tomita
born in Aichi
Oral examination: 4th of February, 2022

The Origin and Regulation of Segmentation Clock Oscillation Dynamics in the Mouse Embryo

Referees: Dr. Aissam Ikmi
Prof. Dr. Christof Niehrs

Abstract

How cells coordinate their dynamic gene expression to produce patterns that transcend to the tissue scale is a fundamental question in biology. In the context of somitogenesis, the timing of segmentation is controlled by a molecular oscillator, the segmentation clock. The segmentation clock oscillations, particularly those regulated by Notch signaling, exhibit traveling wave patterns in the presomitic mesoderm (PSM) due to phase shifted oscillations along the AP axis. How their spatiotemporal dynamics are coordinated to produce such patterns is not fully understood.

I first describe the origin of the traveling waves, with data obtained by imaging the onset of segmentation clock dynamics, at the gastrulating stages of the mouse embryo. Detailed analysis of the oscillations revealed that they are initially synchronous across space at its onset, but accumulate spatial phase shift over the first 6+ cycles, thereby leading to the emergence of traveling wave patterns. Such an accumulation of spatial phase shift agrees with the presence of a period gradient, where period mismatches between adjacent tissue increase the lag in oscillation phase over time.

The existence of an oscillation period gradient has been reported in the later stages of the embryo across species, but not much is known about its regulation. FGF and Wnt signaling gradients present in the PSM have been nominated to control oscillation dynamics. However, past studies have reported that FGF signaling does not affect the segmentation clock, as segmentation pace was unaltered when FGF signaling was perturbed. Using an in vitro model of the PSM also showing an emergence of traveling waves, I characterized the effect of exogenous FGF signal on the wave dynamics in detail. The series of spatially and temporally designed FGF addition experiments indicate that FGF signaling governs the rate of change in oscillation period, or biologically, the rate of cellular maturation towards differentiation. Taken together, I uncover a novel role of FGF signaling in regulating spatiotemporal dynamics of segmentation clock oscillations in the mouse presomitic mesoderm.

Zusammenfassung

Die Koordination dynamischer Genexpression für Expressionsmuster, die über die Zell- zur Gewebsebene hinausgehen, stellt eine fundamentale Frage der Biologie dar. Im Rahmen der Somitogenese wird das Timing dieser Abstimmung der Genexpression von einem molekularen Oszillator bestimmt, der „Segmentation Clock“. Die Oszillationen dieser „Uhr“, besonders jene, die vom Notch-Signalweg kontrolliert werden, zeigen eine wandernde Welle des Signals im präsomitischen Mesoderm (PSM). Diese Signalwelle wird von phasenverschobenen Oszillationen entlang der anterior-posterior (AP) Achse bestimmt. Wie die Oszillationen auf der räumlich-zeitlichen Ebene koordiniert werden, um dieses Wellenmuster zu erzeugen, ist nicht vollständig geklärt.

In dieser Arbeit beschreibe ich zuerst den Ursprung der wandernden Signalwellen anhand von Daten, die durch die Beobachtung des Einsetzens der „Segmentation Clock“-Dynamiken in Mausembryonen während der Gastrulation generiert wurden. Eine ausführliche Analyse der Oszillationen zeigte, dass diese bei ihrer Entstehung zuerst synchron verlaufen, aber über die ersten sechs und mehr Zyklen eine räumliche Phasenverschiebung akkumulieren und es so zum Aufkommen des wandernden Wellenmusters kommt. Solch eine Ansammlung von räumlicher Phasenverschiebung stimmt mit dem Vorhandensein eines Periodengradienten überein, in dem die Unterschiede in der Periode zwischen benachbarten Geweben die Verschiebung der Oszillationsphase vergrößern.

Die Existenz eines Periodengradienten in der Oszillation wurde in späteren Entwicklungsstadien über Spezies hinweg gezeigt, jedoch ist wenig über dessen Regulierung bekannt. Signalgradienten der Wnt- und Fibroblasten-Wachstumsfaktor-Signalwege („fibroblast growth factor“, FGF) im PSM sind Kandidaten für die Kontrolle der Oszillationsdynamik. Jedoch haben vergangene Studien gezeigt, dass der FGF-Signalweg die „Segmentation Clock“ nicht beeinflusst, da die Segmentierungsgeschwindigkeit bei Störung des FGF-Signals unverändert blieb. Mithilfe eines in vitro PSM-Modells, welches auch das Aufkommen wandernder Signalwellen zeigt, habe ich den Effekt von exogenem FGF-Signal auf die Dynamik der Wellen ausführlich charakterisiert. Die Reihe von Experimenten mit räumlicher und zeitlich verschiedener FGF-Zugabe offenbart, dass der FGF-Signalweg die Änderungsrate der Periode bestimmt, oder auf biologischer Ebene, die Geschwindigkeit der Zellreifung hin zur Zelldifferenzierung. Zusammenfassend identifiziere ich eine neue Rolle des FGF-Signalwegs in der Regulation der räumlich-zeitlichen Oszillationsdynamik der „Segmentation Clock“ im PSM der Maus.

Acknowledgements

First I would like to thank my supervisor Alexander Aulehla, for allowing me to pursue science in his group and for guiding me throughout the four years that I have spent at EMBL. From Alexander, I have learned the importance to zoom out, to look at the bigger picture. I am very grateful for his efforts and commitments to nurture me as a scientist, for his encouragement during the tough times, and for giving me the freedom to seek my interests to the end of my satisfaction.

I want to thank Aissam Ikmi and Christof Niehrs for their kind support and advice for my project as members of my thesis advisory committee, and as the first and second examiners of my thesis. Thank you to Jamie Hackett for always providing me with detailed feedback and encouragement as a member of my thesis advisory committee and examination committee. Thank you to Ulrich Schwarz for accepting to be on my examination committee. I want to thank Ryoichiro Kageyama for bringing me into the world of oscillations, for supporting me throughout my challenge to pursue science abroad, and for providing insight as a member of my thesis advisory committee. I am grateful to the members of the Kageyama lab who greet me with kindness when I have the chance to visit. I want to thank Takashi Hiiragi for watching over me, fuelling me with energy and confidence when I most needed it.

I would like to thank all the members of the Aulehla lab, for including me in such a friendly environment. I want to thank Henning Falk for his patient guidance during my first years, Gregor Mönke for introducing me to the interface between theory, biology, and coding, Carina Vibe for discussions that deepened my understanding of the α model, and Paul Gerald Layague Sanchez for sharing the Woods Hole spirit with me. Thank you, Jana Fuß for your help in translating my abstract to German. I want to thank Nobuko, Ivica, and Ana for their tireless efforts that keep the lab going. Thank you to Silvija Svambaryte for enduring me as a lab mate, batchmate, and flatmate.

I want to thank Paul François and Victoria Mochulska for extensive discussions on applying theory to my experiment results. I want to thank Rob Phillips, Jané Kondev, Julie Theriot, and Hernan Garcia for a transformative experience at Woods Hole. Thank you to the lab members of the Hiiragi lab and Ikmi lab, whom I visit most often to seek help for technical issues. The joint lab meetings were always stimulating and I have enjoyed them greatly.

I am grateful to the Takenaka Scholarship Foundation for providing me with partial financial funding and continuous moral support, reinforcing my motivation to succeed and eventually pay forward.

I want to thank all the members of Laboratory Animal Resources for their endless support, members of the ALMF for maintaining the microscopes crucial for my project, and the Kitchen ladies for always keeping the shelves full.

Thank you to my closest friends in Heidelberg: Nobuko, Hidenobu, Emilia, Carina, Paul, Silvija, Jona, Anniek, Takafumi, and Marie, for helping me out in the toughest of times and making

my journey abroad such a meaningful experience. Thank you to my parents, who gave me the freedom to follow my passion, and supported me unconditionally, to my sister and her family for sharing photos and videos that brighten my day, and to Kurosuke, for being a warm and welcoming brother.

I want to end by thanking Mami, who has given me joy and power over the years. Thank you for choosing to come to Germany and for supporting me every day. I am very lucky to have you by my side.

Table of Contents

List of Figures

Part I

Introduction

CHAPTER 1

Somitogenesis and the segmentation clock

1.1 The clock and wavefront model and its biological correspondents

In vertebrate development, axial segmentation occurs concurrently with axial elongation, progressing sequentially in the rostrocaudal direction. Somites, the precursor of vertebrae, are cleaved off in pairs from the presomitic mesoderm (PSM) at the rostral end, while this tissue elongates caudally. Proper segmentation at the developmental stage is critical for achieving correct structure of axial skeletons [Eckalbar et al. (2012)]. This periodic process occurs with remarkable spatiotemporal precision, attracting theoretical and experimental interest over the last few decades.

Before the advent of genetic tools, [Cooke and Zeeman (1976)] proposed the clock and wavefront model, which is to date the most widely known model in the field of somitogenesis. This model postulates a cellular oscillator that is synchronous across the PSM, and a moving front of rapid cell change traversing the tissue in anterior to posterior direction. With each oscillation, cells anterior to the moving front are allowed to differentiate into a somite. Thus, new somites are made successively, at the period of the oscillator. In this scenario, each cell senses the wavefront, which also instructs the arrest of oscillations. Investigations have been made using this model as a guide, to uncover the molecular identity of the clock and wavefront. I detail the history of its discoveries below.

1.1.1 Molecular oscillators in the PSM

[Palmeirim et al. (1997)] first confirmed the existence of a molecular oscillator in the chick PSM. The expression of *c-hairy1* showed wavelike propagation from the posterior tailbud to the anterior edge of the PSM, in 90 minute cycles corresponding to segmentation pace. Importantly, it was shown that these waves are phase waves, and not caused by propagating signal from the posterior, sequentially activating *c-hairy1* expression in each cell. In fact, each cell acts as an individual oscillator, with its phases slightly shifted across space. This creates the impression of traveling waves across the PSM.

Similarly, *Hes1* and *Hes7* in mouse, and *her1* and *her7* in zebrafish, was shown to be cyclically expressed in the PSM, also exhibiting a traveling wave pattern from the posterior to anterior [Jouve et al. (2002); Bessho et al. (2001); Holley et al. (2000); Oates and Ho (2002)]. These genes are of the same *hairy-Enhancer of split* class of basic helix-loop-helix (bHLH) transcription factors, and receives input from the Notch signaling pathway [Jouve et al. (2002)]. *L-fng* expression was also shown to oscillate in chick and mouse, adding to the list of cyclic genes in the Notch pathway [Aulehla and Johnson (1999); Forsberg et al. (1998); McGrew et al. (1998)]. Importantly, it was shown that the Hes genes are able to repress its own expression, forming a negative feedback loop responsible for its oscillatory expression [Bessho et al. (2003); Lewis (2003)]. Since then, expression of genes in the Wnt and FGF pathways have also been shown to oscillate in the mouse PSM. [Aulehla et al. (2003); Dale et al. (2006); Dequéant et al. (2006)]

Real time reporters of these cyclically expressed genes greatly facilitated the scrutinization of its oscillation dynamics. Chemiluminescent and fluorescent reporters for various oscillatory genes in mouse, zebrafish and human iPS cells have been engineered, and the list continues to grow [Masamizu et al. (2006); Takashima et al. (2011); Aulehla et al. (2008); Niwa et al. (2011); Shimojo et al. (2016); Delaune et al. (2012); Soroldoni et al. (2014); Yoshioka-Kobayashi et al. (2020); Matsuda et al. (2020); Sonnen et al. (2018) and others]. Importantly, Notch, Wnt, and FGF pathway genes show distinct oscillation dynamics, which will be detailed later. Together, the network of these oscillating genes comprises the segmentation clock, thought to instruct the pace of somitogenesis.

The PSM tissue can then be considered an ensemble of individually oscillating cells. However individual oscillators are prone to noise and are bound to desynchronize over time without additional control. Indeed, oscillations are shown to be coupled intercellularly, through juxtacrine Notch signaling [reviewed in Kageyama et al. (2007)]. Disruption of Notch signaling by the gamma-secretase inhibitor DAPT results in desynchronization of the oscillators, leading to defective segment boundaries [Riedel-Kruse et al. (2007)]. Therefore, the network of cellular coupling is also a vital aspect of the segmentation clock.

Combined, the PSM tissue is able to present coordinated oscillations of the segmentation clock genes. While it is not a single component oscillating synchronously in the PSM as originally postulated in the clock and wavefront model, it is shown to control the timing of segmentation as the clock. As such, the molecular basis of the oscillator as the segmentation clock network is to date well studied and established.

1.1.2 Morphogen gradients in the PSM as the wavefront

Having identified the molecular oscillator, molecules that correspond to the wavefront were then searched for. In this aspect, signaling gradients in the PSM were thought to be fit to play such a role. FGF/Wnt pathway activity is known to be highest at the posterior tailbud, and gradually lower towards the anterior PSM. An opposing gradient of retinoic acid signaling activity also exists, highest at the somites and anterior PSM [Aulehla and Pourquié (2010)]. These signaling gradients are interconnected with each other. FGF and Wnt signaling shows mutually enforcing roles, likely through positive feedback[Aulehla et al. (2003, 2008); Naiche et al. (2011)]. FGF and Retinoic acid pathways are shown to be mutually inhibitory, which is thought to create a sharp transition at the rostral PSM [del Corral et al. (2003)]. Together these gradients could encode positional information which the cells read out as the wavefront.

Indeed, it has been shown that high FGF signaling activity at the posterior tailbud keeps the mesodermal cells at an undifferentiated state. As the axis elongates, anterior cells experience a decline in FGF signaling activity. It was proposed that when cells reach a threshold FGF activity level, they are permitted to differentiate into somites, thereby controlling where the somite boundaries form. Therefore, it was suggested that the wavefront is defined by the position in the PSM with the threshold level of FGF activity. Importantly, it was shown that perturbing FGF signaling did not alter segmentation pace, suggesting that the segmentation clock and wavefront are independent entities [Dubrulle et al. (2001); Sawada et al. (2001)].

The FGF gradient is formed through a time dependent decay mechanism [Dubrulle and Pourquié (2004)]. *fgf8* mRNA transcription is restricted to the tailbud, which stops when cells leave this zone to enter the PSM. Cells experience a gradual decay of the transcript over time, and concurrently moves its relative position to the anterior PSM, as cells rostral to it are continuously cleaved off as somites. This lays out a pattern where rostral cells contain less *fgf8* transcript than caudal cells, thereby creating an *fgf8* mRNA gradient. Assuming a constant translation rate of this mRNA gradient, this process enables the formation of an FGF8 ligand gradient.

This specific mode of FGF gradient formation, combined with the idea that mesoderm cells differentiate at a threshold level of FGF signaling suggests that FGF plays a timer like role. Cells that leave the tailbud will have a fixed amount of time until its transcript/ligand and activity decays to a particular value, when it is allowed to differentiate into a somite.

These studies suggest that indeed functional information for patterning is encoded in the signaling gradients. Together with the molecular oscillator, this could explain somitogenesis in the context of the clock and wavefront model.

1.2 Challenging the clock and wavefront model

The clock and wavefront model seems to precisely capture the phenomenon of somitogenesis. However, there are specific observations that challenge the model. [Lauschke et al. (2013)] presented an explant method of the mouse PSM, where the tailbud of an E10.5 embryo is excised and plated on a fibronectin coated dish. Observing *Lfng* expression dynamics using a fluorescent reporter revealed initially synchronized oscillations across the tissue, which eventually transitioned into waves traveling from the center to the periphery. Strikingly, differentiation into segments occurred sequentially from the periphery. As each wave reached the edge of the tissue, molecular markers of segmentation were activated, and oscillations arrested. In this assay, the tailbud tissue termed "mPSM" for monolayer PSM, recapitulates the AP axis of the PSM in its central periphery axis. Importantly, it was shown that segmentation at the periphery coincided with the position of 2π phase shift in *Lfng* oscillation phase profile, measured from the center of the tissue. The slope of the *Lfng* oscillation phase profile became steeper over time, moving the position of the 2π phase shift inward. This results in a sequential regression of the oscillatory domain, from the periphery inwards.

This assay suggested that the information for segment boundary positioning was encoded in the oscillation phase profile. This scheme provided another explanation of somitogenesis, raising the possibility that oscillation dynamics provide information for space, as well as for timing of segmentation.

The idea that oscillation dynamics encode for segmentation was pursued further in [Sonnen et al. (2018)]. Here, modulation of oscillation phase relationships between the Notch pathway

and Wnt pathway in the mPSM led to postponing the differentiation to segments in these cells. Therefore, it was shown that oscillation dynamics carry functional information for segmentation. These studies challenge the classical clock and wavefront model, represented by a different type of model called the phase shift model [Goodwin and Cohen (1969)]. The phase shift model is a general framework that suggests how temporal information could encode for space. The original paper postulated two waves emitted from a source, a fast S wave, and a slow P wave. Depending on the distance from the source, each position observes different time intervals between the arrival of the two waves. Therefore a cell reads spatial information based on the temporal difference of the two waves. In the context of the PSM, Wnt oscillations and Notch oscillations can correspond to the fast S wave and slow P wave, respectively. The segment boundaries are proposed to form at the intersection of these two waves, using oscillation dynamics to encode for patterning.

In this line of work, it is crucial to understand how the dynamics of the oscillations are regulated. Next, I list the current understandings of the field on segmentation clock oscillation dynamics.

1.3 Oscillation dynamics of the segmentation clock; the period gradient

Of the segmentation clock gene network, Notch pathway oscillations are the most studied and well characterized. In all vertebrate species studied, Notch pathway oscillations exhibit traveling wave patterns progressing from the posterior to the anterior. Even before the arrival of real time reporters, snapshots of the dynamic patterns of oscillatory gene expression were used to deduce the underlying dynamics. Notably, the oscillations exhibit a period gradient across the AP axis. That is, oscillations are fastest at the posterior tailbud and gradually slow down towards the anterior. This arrangement leads to anterior oscillations lagging behind in oscillation phase over time, compared to the posterior-most oscillator. The gradual phase difference across the AP axis then gives the impression that cells activate gene expression sequentially, exhibiting a traveling wave pattern. The spatial phase profiles obtained from gene expression snapshots contain information on how much lag is necessary to produce such patterns. From that information oscillation periods can be deduced at each position. In multiple species including chick, mouse, zebrafish, and snake, estimated period gradients show a concave shape, fitting well to an exponential increase or second-degree polynomial [Palmeirim et al. (1997); Giudicelli et al. (2007); Gomez et al. (2008); Niwa et al. (2011)].

Real time reporters allowed direct measurements of oscillation period, in some cases with single cell resolution. Each confirmed the existence of a period gradient both in mouse and zebrafish PSM [Tsiairis and Aulehla (2016); Shih et al. (2015); Yoshioka-Kobayashi et al. (2020); Rohde et al. (2021)].

The period gradient is a conserved feature of the Notch pathway oscillations across species, and also across contexts. In the previously introduced in vitro mPSM, a period gradient emerges along the central peripheral axis. A priori, we know that cells in the tailbud oscillate with a similar period of about 130 min in mice. Therefore, when cut and plated on glass as an explant, these cells should be oscillating at this period. However, over time, peripheral cells slow down their oscillation period to about 150 minutes while the center keeps oscillating at 130 minutes. The emerging period gradient is phenomenologically responsible for producing phase differences along the central periphery axis, leading to the appearance of traveling waves. Additionally, it has been shown that randomized and reaggregated mouse PSM cells

resynchronize their oscillations to show spatial wave patterns [Tsiairis and Aulehla (2016)]. In this case, multiple foci appear in the tissue, each presenting concentric waves from the center outward. An emergent period gradient of similar amplitude also underlies the formation of these waves.

Therefore the period gradient is a key feature of the Notch pathway oscillations, controlling how the phase differences between neighboring oscillators evolve over time. However, not much is known about how the oscillation periods are regulated across the AP axis. Some studies have suggested that the FGF8 gradient could be regulating oscillation periods in the PSM [Vasiliauskas and Stern (2001); Ishimatsu et al. (2010)], based on fixed stainings of embryos. More recent studies using live reporters have alluded to the effect of FGF activity on the dynamics of segmentation clock oscillations [Diaz-Cuadros et al. (2020)], starting to reveal a new role of FGF signaling in somitogenesis. Here, a more detailed and quantitative study on the relationship between signaling gradients and oscillation dynamics is needed.

1.4 The origin of traveling waves in the presomitic mesoderm

Another open question in the field is the origin of waves in the presomitic mesoderm. Much of the studies focus on developmental stages when the waves are already present, and segmentation is ongoing. A few studies on zebrafish and chick demonstrated fixed stainings at the onset of segmentation clock genes, and reconstructed a time series of the progression [Riedel-Kruse et al. (2007); Jouve et al. (2002); Ishimatsu et al. (2010)]. However, real time reporter imaging at the onset of the segmentation clock has not been performed yet. In the mouse model, this is particularly challenging due to the need to image gastrulating stages of the embryo, before segmentation initiates. A methodology to image these highly photosensitive embryos in toto over 24 hours has only been recently reported, using light-sheet microscopy [Udan et al. (2014); McDole et al. (2018)]. Previous reports described phototoxic effects on development after 10 hours of illumination when a high temporal resolution was used (1.5 min interval), highlighting the photosensitivity of E6.5 mouse embryos [Ichikawa et al. (2013)]. Adapting such techniques to image the onset of segmentation clock dynamics poses a significant challenge but would be crucial to understand how the traveling waves originate in the PSM.

[Riedel-Kruse et al. (2007); Jouve et al. (2002)] both report the presence of a traveling wave at the onset of segmentation clock oscillations in zebrafish and chick, respectively. That is, the earliest observed activation already shows spatially phase shifted patterns across the embryo. In zebrafish, the earliest expression of cyclic genes is observed at ~5.25 hours postfertilization (hpf) at around 50% epiboly. *dlc* expression is reported to start from the ventral side and move to the dorsal side, showing a traveling wave. At 8.2hpf, waves start to travel from posterior to anterior and continue this propagation pattern. Interestingly, horizontal waves traversing in the ventral to dorsal direction was not observed in a following study focused on *her1* expression [Ishimatsu et al. (2010)]. This highlights the importance of live imaging the dynamics of these genes to resolve such discrepancies. In chick, cyclic expression of *c-hairy2* and *lunatic fringe* is first observed at Hamburger and Hamilton (HH) stages between HH3+ and HH4-, correlated in timing with the ingression of paraxial mesoderm. The expression starts at the caudal primitive streak, and undergoes movement toward the anterior, presenting a traveling wave. The dynamics of the first and second waves are reported to be different in terms of progression speed. While the first wave takes 5 hours to complete, the second wave finishes its migration in about an hour. Additionally, the first two waves do not result in the

formation of somites. In contrast, in zebrafish, there are five oscillations that do not result in a somite, as the sixth cycle prefigures the first segment boundary[Riedel-Kruse et al. (2007)].

Real time quantifications at the onset of segmentation clock oscillations would answer open questions such as; when is the period gradient first observed? If oscillation dynamics encode for segmentation, what is the relationship between the dynamics of the earliest waves, and their ability to produce boundaries? In part II I describe how we tackled this problem in the gastrulating mouse embryo, and detail the oscillation dynamics observed.

Part II

The onset of segmentation clock oscillations in the gastrulating mouse embryo

CHAPTER 2

Background

2.1 Establishing a technique to image the onset of segmentation clock oscillations

In order to visualize the origin of segmentation clock oscillations in the mouse model, Henning Falk, a previous Ph.D. student spearheaded the development of utilizing the Zeiss Z.1 microscope to culture and image E6.5 to E8.5 mouse embryos (Fig. 2.1A). Lightsheet imaging offers fast volumetric imaging with reduced phototoxicity in comparison to confocal or multi-photon imaging [Keller et al. (2008); Ichikawa et al. (2013); Udan et al. (2014); McDole et al. (2018)]. Since mouse embryos at the gastrulating stages are extremely photosensitive and additionally undergo roughly a 100x fold increase in volume during the E6.5-E8.5 stages, light-sheet imaging was chosen as the suitable mode of visualization.

Henning Falk established a system to allow circulated perfusion of temperature/gas controlled medium through the imaging chamber of the Zeiss Z.1 microscope. Additionally, he designed a smaller chamber that can be fitted inside the standard Z.1 chamber, allowing the frequent exchange of medium through circulation and thus achieving a tighter environmental control (Fig. 2.1B). The smaller chamber also adds the benefit of reducing medium usage (~30ml to ~4ml), satisfying an ethical and economical motive to reduce the amount of rat serum necessary for culture. He also devised a method of mounting the embryos in a capillary, by holding the ectoplacental cone in the agarose while not constraining the rest of the embryo. This configuration allows the embryo to grow and expand freely in the medium during culture and imaging (Fig. 2.1C).

Combined, he successfully cultured mouse embryos across E6.5 to E8.5 stages on the Z.1 microscope (Fig. 2.1D), and was able to image them for over 40 hours. In addition, he designed a multi-sample capillary holder (SPIM-for-4) which enables the imaging of four samples in one experiment (Fig. 2.1E,F). It uses the rotation axis of the Z.1 system to change sample positions and therefore sacrifices the rotational regulation of each sample. However since our primary objective was to visualize segmentation clock dynamics occurring at the posterior half of the embryo, rotation of each sample was dispensable. This allowed higher throughput and also an ability to reliably compare control and experimental embryos in the same imaging experiment.

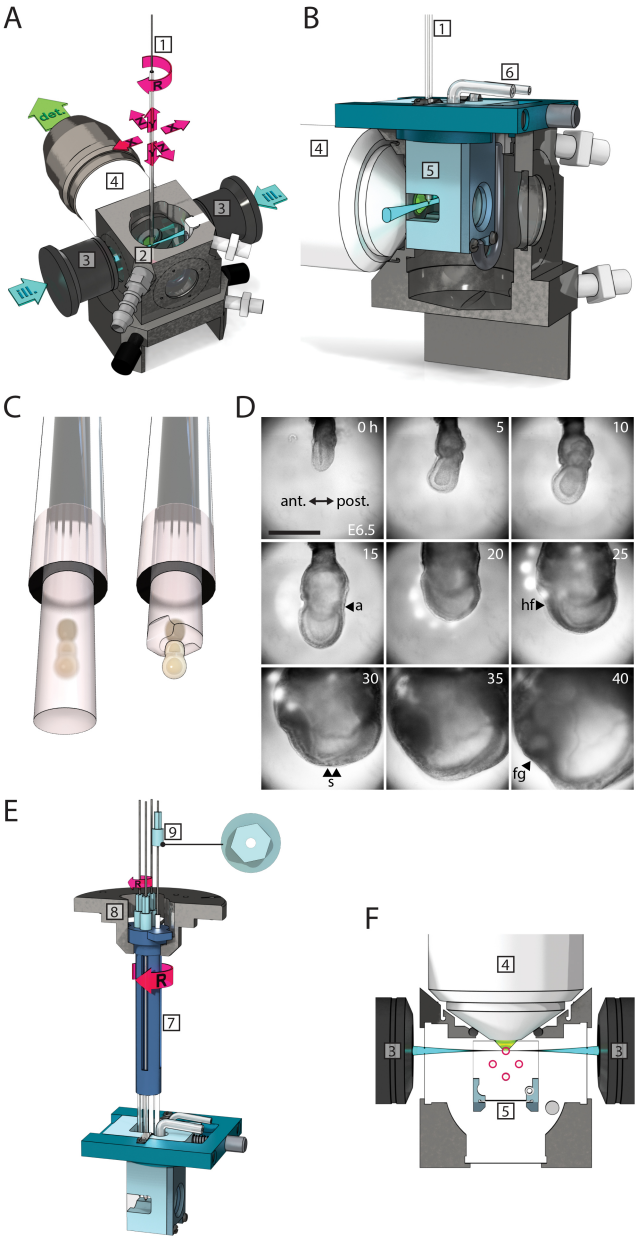

Figure 2.1: This figure and legend has been adapted from [Falk (2018)] with permission from Henning Falk. "**Light-sheet microscopy for multi-sample live imaging of mouse embryos from gastrulation to organogenesis.** (A) Imaging chamber and objective configuration of the Lightsheet Z.1 (Carl Zeiss) with two illumination light-sheets (ill.) and one detection light path (det). The sample-containing capillary (1) is suspended from the top into the imaging chamber (2) and orientated with respect to the illumination (3) and detection objectives (4); degrees of freedom indicated by red arrows; XYZ, translation; R, rotation). (B) Vertical section view through the sample chamber with inserted embryo culture chamber (5). The embryo culture chamber consists of a chamber lid (dark blue) and the chamber body (light blue) with membrane-covered windows for the light paths. It is connected via tubes (6) to the closed-cycle perfusion system of the microscope. (C) For mounting, embryos were first agarose-embedded in a capillary (left), then the agarose was peeled off around the embryo, leaving only the ectoplacental cone embedded to allow growth during culture (right). (D) Bright-field images of an embryo developing on the customized light-sheet microscope (anterior to the left). The experiment starts at mid-streak stage at E6.5. Morphological features are the allantois (a), the head fold (hf), somites (s), and foregut pocket (fg). Scale bar: 500 µm.

Figure 2.1: (E) SPIM-for-4 multi-sample holder. Four sample capillaries are positioned in the sample holder (7), which is mounted on the Z.1 stage using the standard sample holder disc for syringes (8). A capillary cap is glued to the top of each capillary (9; in top view on the right). With a hex key, each capillary can be turned individually around its long axis (small R) while the rotation drive of the microscope stage allows for switching between samples (large R). (F) Horizontal section view through the imaging chamber in the plane of the light path. Sample capillaries (red circles) in the SPIM-for-4 multi-sample holder do not interfere with the light paths during imaging and the holder is compatible with the embryo culture chamber. *CAD drawings of Z.1 microscope parts provided by courtesy of Carl Zeiss Microscopy GmbH.* [Falk (2018)]" Experiments performed and figures made by Henning Falk.

2.2 Imaging the onset of segmentation clock oscillations using the LuVeLu reporter

Henning Falk used the established system to image E6.5 mouse embryos expressing the LuVeLu reporter, a reporter of *Lfng* expression reflecting Notch signaling activity [Aulehla et al. (2008)]. Here he found that the onset of oscillatory gene activity starts shortly after gastrulation, around E7.0, or at the early allantois bud stage. At the beginning of gastrulation, cells of the epiblast at the primitive streak begin to ingress as the first mesodermal cells. These cells are seen to have a weak expression of the LuVeLu gene, directly after EMT and not before. As the mesodermal "wings" cover the posterior half of the embryo [Downs and Davies (1993)], there is a timing where all the LuVeLu positive cells upregulate its expression simultaneously. We refer to this phenomenon as the "pulse", which is the first synchronous event of LuVeLu gene expression that we observe. Oscillatory gene activity ensues ~4.5 hours after the peak of the "pulse", with a periodicity of ~145 min (Fig. 2.2A). Traveling waves are seen to occur from the primitive streak to the distal regions of the left and right mesodermal wings (Fig. 2.2C).

Henning Falk observed that the pulse was qualitatively and quantitatively distinct from the following oscillations. First, the strength of expression at the peak was ~2 fold higher in the pulse compared to the oscillations. Second, the time interval between the pulse peak to the first oscillation peak was around ~4.5 hours, which was ~2 fold longer than the subsequent peak to peak interval. Therefore, he concluded that the pulse should be distinguished from the latter oscillations as a "pre-clock" phase.

Henning Falk also checked that the pulse was not an artifact of the LuVeLu construct by staining for endogenous *Lfng* expression in freshly dissected embryos. Endogenous *Lfng* expression in embryos during the mid-streak to early headfold stages was visualized using in situ hybridization (Fig. 2.2B), and a time series was reconstructed according to their developmental stage. It was confirmed that *Lfng* exhibits strong global expression at the early bud stage, indicating that the pulse is not a culture artifact or a phenomenon limited to the LuVeLu reporter. Variable expression patterns of *Lfng* were observed for samples in the late allantois bud stages, indicative of dynamic oscillatory expression of *Lfng*. Therefore, the endogenous *Lfng* expression patterns agreed with the dynamic LuVeLu expression patterns observed on the SPIM. This indicated that LuVeLu can be used as a reporter of *Lfng* expression at the onset of segmentation clock dynamics.

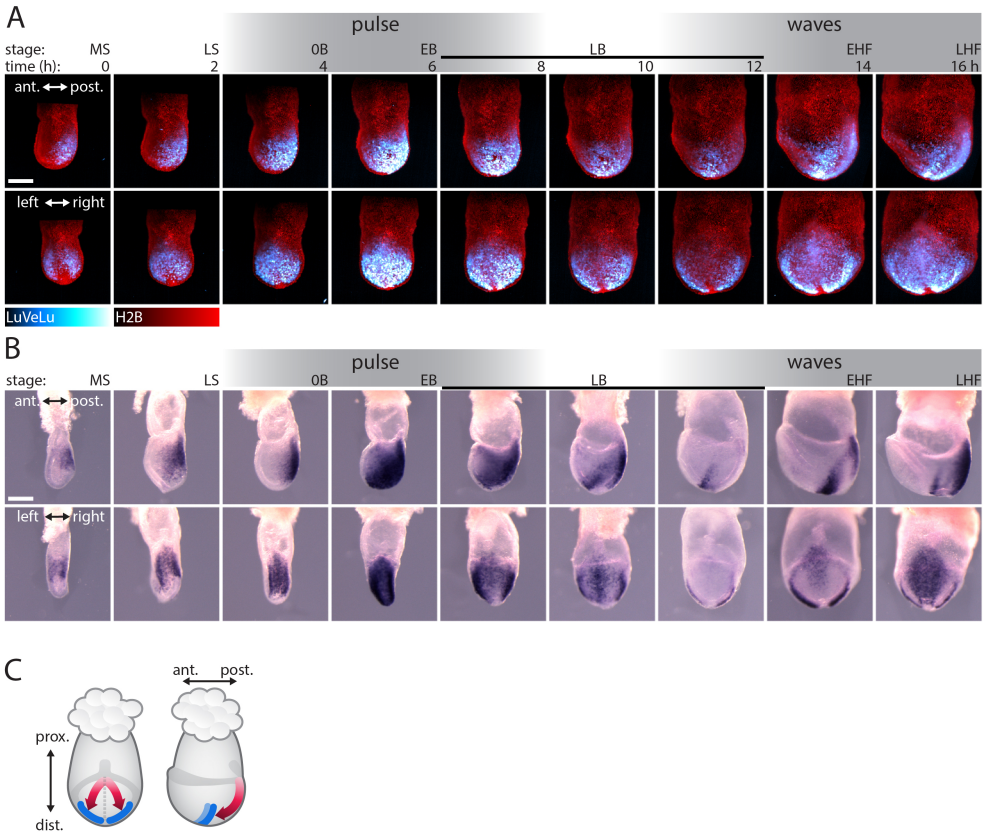

Figure 2.2: This figure and legend has been adapted from [Falk (2018)] with permission from Henning Falk. "**Spatiotemporal expression dynamics of *Lfng* from gastrulation to onset of somitogenesis.** (A) Still frames of a representative LuVeLu;R26-H2BmCherry embryo imaged for 35 h starting at early gastrulation (n=12 similarly imaged embryos). Image stacks are shown as maximum intensity projection (MIP) from the side (top) and from posterior (bottom). LuVeLu shows an intensity pulse after 6 h and traveling waves become visible after 14 h. Embryo stages according to Downs and Davies (1993) are listed above (mid streak, MS; late streak, LS; no allantois bud, 0B; early allantois bud, EB; late allantois bud, LB; early head fold, EHF; late head fold, LHF). (B) Reconstructed time series of *Lfng* mRNA expression between E6.5 and E8.5. The same embryos are shown in a side view (top) and from posterior (bottom). Number of samples collected for the different stages: MS: 9, LS: 6, 0B: 8, EB: 10, LB(1): 16, LB(2): 6, LB(3): 28, EHF: 2, LHF: 2, somites: 8. (C) Cartoon of E7.5 embryo in posterior view (left) and side view (right) to illustrate the domain and directionality of early waves (red arrows) in paraxial mesoderm (PS, dotted line). Early somite boundaries are depicted in blue. All scale bars: 200 µm. [Falk (2018)]" Experiments performed and figures made by Henning Falk.

Aims of the study

Henning Falk developed a method to visualize segmentation clock dynamics at its onset in the gastrulating mouse embryo.

In this part I address the following questions:

1. What is the quality of embryos after culture/imaging using this method? Are there impacts to embryo development?

2. What are the quantitative dynamics at the onset of segmentation clock oscillations?

3. When is the period gradient first observed?

I perform imaging of E7.5 mouse embryos expressing the LuVeLu reporter, and compare its outcome to that of standard methods of roller culture to assess sample health. I devise a computational pipeline to properly extract oscillation dynamics from the curved surface of the embryo, which allows a precise description of the emergence of traveling waves. I transfer cellular movement data from [McDole et al. (2018)] to obtain cellular flows, enabling me to question whether a cellular period gradient is present. Combined, the data shows that a period gradient is present already at the onset of segmentation clock oscillations.

CHAPTER 3

Results

3.1 Validation of the culture and imaging protocol

While morphological landmarks (e.g. neural tube, segment boundary, head fold, allantois) were visualized to occur correctly during culture in the Z.1 microscope, phototoxicity had not been assessed in detail. With the imaging protocol necessary to visualize the dynamics in the LuVeLu reporter, I checked its impact on the development of the embryos by assessing morphological and molecular markers of posterior patterning. I stained embryos cultured for 24 hours (E7.5-E8.5) on the Z.1, either imaged or not imaged, on the roller culture, and those freshly dissected at E8.5 for the genes Uncx4.1 (marking caudal half of somites), Shh (marking floor plate of neural tube), and Msgn (marking presomitic mesoderm) (Fig. 3.1A). The imaging settings used was identical to that for LuVeLu imaging [Z-stacks with 7.5 µm spacing, 100 slices per sample, 300 ms exposure time with 2.0% 50mW 514nm laser and 10 min imaging interval.], which is a relatively high dosage of light necessary to visualize the dynamic reporter.

Comparing the resulting embryos revealed that the culture in the Z.1 system (non-imaged embryos) was comparable to that of roller culture and in utero development. However, we did observe compromised axis elongation for the imaged embryos, likely due to phototoxicity. The imaged embryos showed wider, narrowly spaced segments compared to the other conditions, as well as a shorter and wider PSM region.

Culture outcome was compared by counting the number of Uncx4.1 stripes seen in the embryos as a proxy of developmental progression. No significant difference was seen between the number of Uncx4.1 stripes observed after culture, suggesting that segmentation is not delayed by imaging or culturing the samples in the Z.1 system (Fig. 3.1B).

Therefore, I concluded that culturing in the Z.1 system is at least comparable to standard roller culture. However, phototoxicity is observed when imaging for the LuVeLu reporter with the chosen settings, highlighting the sensitivity of the embryos at this stage.

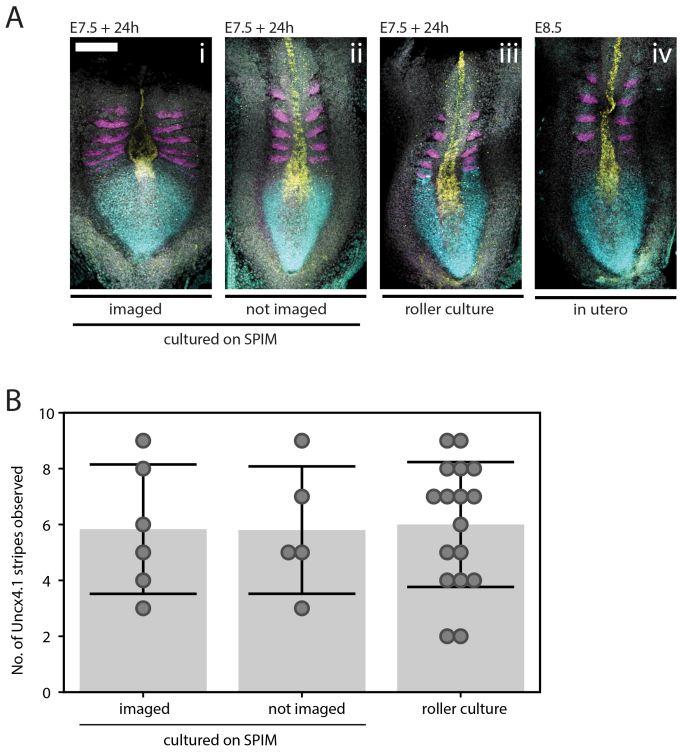

Figure 3.1: The text for this legend has been originally written by Takehito Tomita and taken from [Falk et al. (2021)] in revision. "**Validation of the culture and imaging protocol on the Zeiss Z.1 microscope** (A) (E) Examples of embryos after culture on the microscope: (i) imaged for the LuVeLu reporter (Z-stacks with 7.5 µm spacing, 100 slices per sample, 300 msec exposure time and 10 min imaging interval. n=6).(ii) SPIM-cultured without imaging (n=5). (iii) roller-culture (n=17) and (iv)*in utero* developed control embryos dissected at E8.5 (n=12). For all embryos a hybridization-chain reaction (HCR) based in situ mRNA hybridization was performed for the following genes: *Msgn1* (cyan), a marker for presomitic mesoderm, *Shh* (yellow), expressed in notochord and the floor plate of the neural tube, and *Uncx4.1* (magenta), marking the anterior-posterior subdivisions of the somites. Scale bar 200 µm. (B) Bar plot showing the number of Uncx4.1 stripes observed in embryos either SPIM-imaged (mean:5.83, n=6), cultured in SPIM but not imaged (mean:5.8, n=5), and cultured in roller culture (mean:6.0, n=17). Embryos were dissected at E7.5 and cultured for 24 hours. Bar plot shows the mean value of samples within each group, error bars show standard deviation." Experiments performed and figures made by Takehito Tomita.

3.2 The development of wave dynamics at the onset of segmentation clock oscillations

I further examined how traveling wave patterns of LuVeLu expression originate in the mouse embryo. It was necessary to take into account that the waves traveled along the curved surface of the embryo, and to this end, I developed a pipeline to generate kymographs with a 3D+t line of interest following the surface of the embryo. This line of interest starts at the proximal wave origin and extends to the distal edges of the mesoderm, and follows this dynamically over time (Fig. 3.2A, Movie 1). LuVeLu signal intensity is picked up along this line for each timepoint, and the spatial intensity profiles are then stacked to generate a kymograph, a spatiotemporal representation of LuVeLu expression dynamics (Fig. 3.2B). Importantly, the

spatial axis on this kymograph correctly represents the distance the waves travel on the surface of the embryo.

To obtain quantitative information on the oscillation dynamics, the LuVeLu kymographs were converted into phase kymographs using the wavelet transform (Fig. 3.2C). The phase profile across space at each timepoint was then used to obtain the wave number, or how many waves span the oscillatory domain. In the E10.5 mouse embryo, a full wave is observed in the PSM, and therefore the wave number is ~1 [Takashima et al. (2011); Aulehla et al. (2008)]. Our quantifications revealed that at the onset of wave dynamics, the wave number is close to zero, and only gradually increases towards one (Fig. 3.2E). I also measured the average phase difference per unit length, by dividing the wave number by the oscillatory field length (Fig. 3.2D), and used this as a linear estimate of the phase gradient slope (Fig. 3.2F). This slope value also increased monotonously during the first oscillations, indicating that oscillations are initially in synchrony, but gradually accumulate phase differences between each position, leading to the appearance of traveling waves. From this result, I can deduce that oscillations occur with different periods at different locations in the early mesoderm. Specifically, distal oscillations are slower than the proximal oscillations, therefore accumulating phase differences over the oscillation cycles. This indicates that a tissue level oscillation period gradient is already present at the very first cycles of the mouse segmentation clock, and is the phenomenological basis for gradually building up the traveling waves to sweep across the mesoderm.

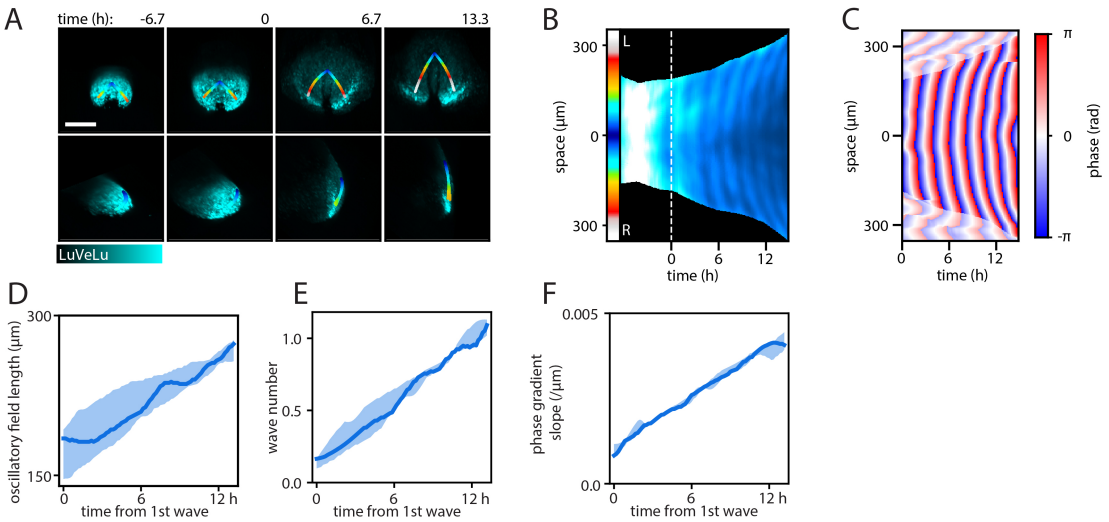

Figure 3.2: The text for this legend has been taken from [Falk et al. (2021)] in revision. **"Phase dynamics of LuVeLu oscillations during the first waves.** (A) Still frames of a representative LuVeLu embryo and the line of interest following the curved surface of the mesoderm. Imaged for 20+h starting at no allantois bud stage (n=5 similarly imaged embryos). Image stacks are shown as maximum intensity projection (MIP) from the posterior (top) and from side (bottom). Scale bar: 200 µm. (B) Intensity kymograph along the line of interest shown in (A). The proximal region is registered at the center of the kymograph, while the left and right distal ends extend above and below, respectively. Timepoint zero is set when the first wave is observed, represented by the white dashed line. (C) Corresponding phase kymograph made by analyzing intensity time series in (B) with Wavelets. Shaded region represents region outside of the kymograph, corresponding to black regions in (B). (D) Length of the LuVeLu oscillatory field measured along the line of interest following the surface of the mesoderm, from the proximal oscillation origin to the distal end. (E) Total phase shift within the mesoderm from proximal to distal, quantified as wave number q (q=1: one wave is visible within the entire mesoderm field). (F) The linear estimate of phase gradient slope, obtained by dividing the wave number by oscillatory field length at each timepoint. (C–E) Solid lines represent median, corridors mark IQR." Experiments performed and figures made by Takehito Tomita.

3.3 Utilizing data from [McDole et al. (2018)] suggests that a period gradient is present at a cellular level at the onset of segmentation clock oscillations

In addition to a tissue level period gradient, I pursued to check whether a period gradient is present at a cellular level. The most direct method to determine this is to track single cell oscillations and measure the periods at different locations. Henning Falk and I pursued this direction to track single cells using mosaic labeling strategies. However, we were not able to find a suitable imaging condition that allowed both tracking and acceptable standards of embryo development. The phototoxicity was generally too high for these conditions, especially as imaging for the LuVeLu reporter already requires a high light dosage.

Therefore I took an alternative approach to utilize the data presented in [McDole et al. (2018)], where single cell tracking was performed in toto during the E6.5-E8.5 stage mouse embryo. I stage matched their tracking data from four embryos to our dataset and determined the timepoint which would correspond to the onset of segmentation clock oscillations. This was

done using the size of the embryo and the extent of mesoderm ingression as a proxy of the developmental stage. I then proceeded to align the 3D+t line of interest onto the tracking data similarly as I did for our datasets, to obtain cell movement from the corresponding regions (Fig 3.3A, Movie 2). The cell tracks observed in the line of interest in four embryo datasets were projected in the same orientation as the LuVeLu kymographs, and their vectors were averaged into streamlines which represent the flow of cells (Fig 3.3B). The vector fields from the four embryos were then averaged into one streamline plot, showing the mean cellular flow in these embryos (Fig. 3.3C). The observed flow suggested that the mesodermal cells follow a proportional expansion of the tissue. This observation was in agreement with the decrease in cell density which was extracted from the cell track data (Fig. 3.3D).

The decrease in cell density in combination with the increase in phase gradient slope discussed earlier suggests that there is a cellular period gradient in the mesoderm. To explain, let us consider an array of n oscillators which have phase values $\phi_1(t)$~$\phi_n(t)$. For a traveling wave to be observed, $\phi_1(t) < \phi_2(t) ... < \phi_n(t)$. We let the number of oscillators vary over time as $n(t)$ and the total spatial length of the array as $l(t)$. Density is then given by $n(t)/l(t)$.

We have estimated the linear phase gradient slope by dividing the wave number by the length of the oscillatory field, which in our model would be given by $s(t) = \frac{\phi_n(t)-\phi_1(t)}{l(t)}$. On the other hand, the average cellular phase difference is given by $p(t) = \frac{\phi_n(t)-\phi_1(t)}{n(t)}$. These two quantities are related through density by $p(t) = \frac{s(t)}{n(t)/l(t)}$. The temporal increase in the phase gradient slope $s(t)$ with a decrease in density $n(t)/l(t)$ ensures that $p(t)$ increases over time. Therefore, on average, neighbouring cells increase their phase differences over time, arguing for a period mismatch among them. This suggests that if single cell oscillations were to be captured, their oscillation periods would be graded from the proximal wave origin to the distal ends.

The logic above argues for the existence of a period gradient at the cellular level. To augment this, I reasoned that the cellular flow streamlines can be overlaid to the LuVeLu kymographs, then be used to extract oscillations attributed to the same group of cells. Since the streamlines diverge radially, I interpolated between the proximal and distal trajectories to obtain 10 tracks that should follow the same group of cells. These tracks were overlaid on the LuVeLu kymographs and the intensity time series were obtained for each of the tracks (Fig. 3.3E). The oscillation periods extracted from these time series indeed show a graded distribution from proximal (median 133 min, IQR 7.67 min) to distal (median 152 min, IQR 10.3 min), supporting the hypothesis that at the onset of segmentation clock oscillations, cells already exhibit different periods according to their position (Fig. 3.3F).

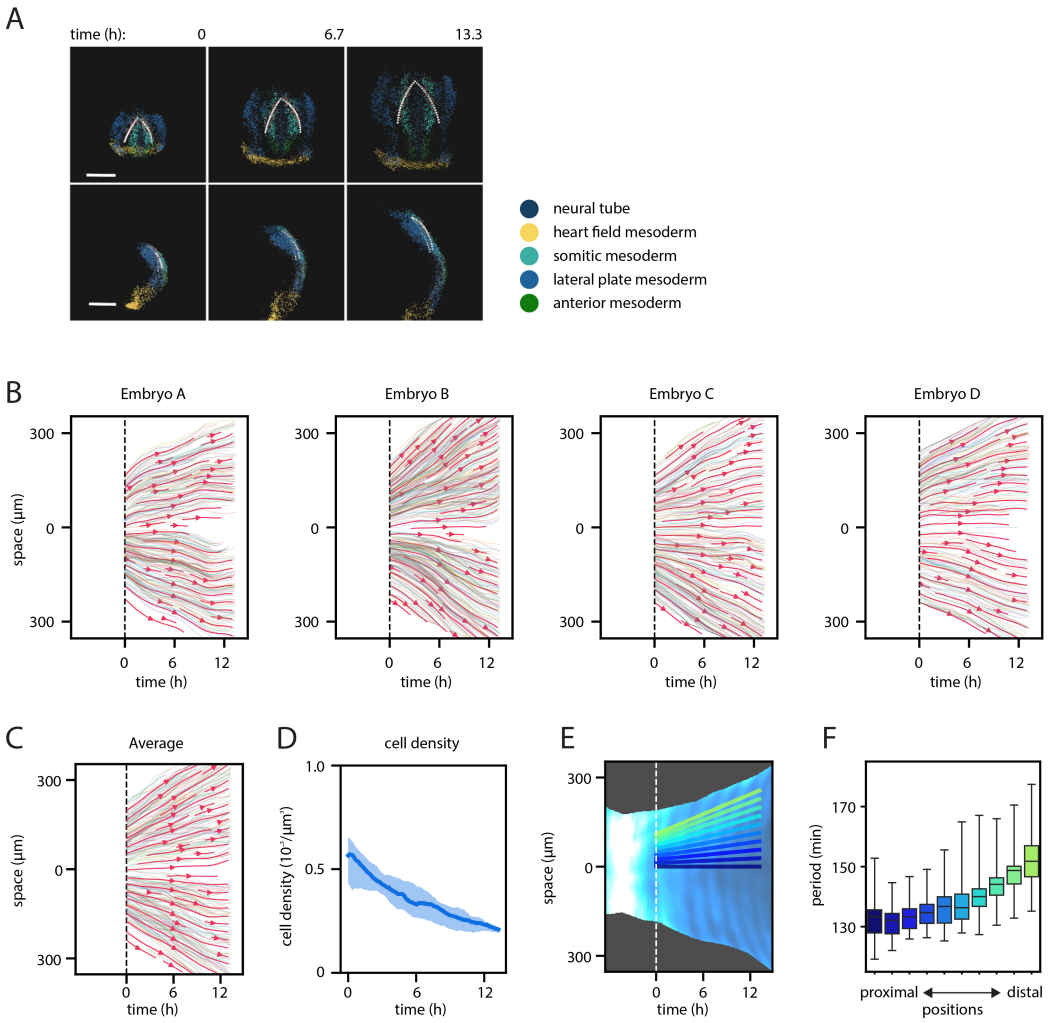

Figure 3.3: The text for this legend has been originally written by Takehito Tomita and taken from [Falk et al. (2021)] in revision. **"Utilizing data from [McDole et al. (2018)] to obtain period dynamics.** (A) Still frames of cell tracking data from [McDole et al. (2018)] and the transferred line of interest following the curved surface of the mesoderm (n=4 datasets). Image stacks are shown from the posterior view (top) and from side view (bottom). Cell locations in the cell tracking datasets are represented as octahedrons color coded with the cell fate annotations in the legend. The transferred line of interest used to generate cell track/flow plots (B–C) is represented as a line of white spheres. Cells within 30 µm of the line of interest are colored red. The datasets are aligned so that t=0 is set to the timepoint which corresponds to the start of the first wave. Scale bar: 200 µm. (B) Streamline plot showing the flow of cells, based on cell tracks obtained from four mouse embryo datasets, shown individually. The proximal region is registered at the center, while the left and right distal ends extend above and below, respectively. Each shaded line represents a single cell track. Annotated mesoderm cells staying within the 30 µm radius of the line of interest for more than 300 min were included for analysis. 1/2 of the set of cell tracks are visualized per embryo. (C) Averaged streamline plot showing the flow of cells of four embryos. Vector fields obtained from each embryo were averaged to draw the streamlines. 1/8 of the entire set of single cell tracks are visualized as shaded lines. (D) Cell density measured in the volume within the 30 µm radius of the line of interest on the cell tracking datasets. All annotated mesoderm cells in this zone were considered for each timepoint, for left and right sides of the embryo treated independently as a sample. Solid lines represent median, corridors mark IQR.

Figure 3.3: (E) Interpolated cellular flow lines to obtain oscillations from the LuVeLu kymographs. The same set of lines were used to obtain 10 tracks of oscillation time series per embryo, from proximal to distal. (F) Period measurements obtained from the oscillation time series obtained from tracks shown in (E). Period values were collected from timepoints 120 min to 360 min from the start of the waves, corresponding to the second and third waves. Color coding of boxes corresponds to the lines shown in (E). Boxes represent IQR, whiskers extend to the minimum and maximum values." Experimental data taken from [McDole et al. (2018)]. Data analysed by and figures made by Takehito Tomita.

CHAPTER 4

Discussion

4.1 Limitations in the current imaging protocol

In section 3.1, I showed that phototoxic effects are observed when embryos are imaged from E7.5 to E8.5, using the conditions necessary for LuVeLu imaging. Axial elongation is compromised, and somites are seen to be wider and shortly spaced. This does raise the question as to how much the observed signaling dynamics represent endogenous behavior. Key features such as the *Lfng* pulse and subsequent occurrence of dynamic expression are qualitatively confirmed by in situ hybridization of freshly dissected embryos. Evidence of developmental retardation is also not observed, as imaged embryos show statistically similar numbers of segments as their non imaged littermates. However, quantitative details, such as values of the phase gradient slope, could be compromised especially as it incorporates measurements of oscillatory field length. Related to this, it is unclear if, and to what extent transferring cell movement data from [McDole et al. (2018)] can be justified.

Since the culture in the Z.1 microscope itself is comparable to the well established roller culture technique, reduction of photon exposure seems to be key to resolve this issue. I have not tested the lower limits of fluorescent excitation that allow robust detection of signaling dynamics. Decreasing z spatial resolution by 2 fold and temporal resolution by 1.5 fold can already achieve a 3 fold reduction in photon exposure. Laser intensity and exposure time can also be slightly lowered to 75% of the current settings. Combining such optimization could alleviate the phototoxic effects. In addition, we should pursue the usage of further optimized fluorescent proteins. Specifically, the Achilles protein mutagenized from Venus shows a faster maturation rate and is shown to be suitable for visualizing dynamically expressed genes [Yoshioka-Kobayashi et al. (2020)].

Both Henning Falk and I have attempted to track single cells of the gastrulating mouse embryo using the Z.1, to obtain cellular oscillation dynamics. To date, we have not yet succeeded, but it is of great interest to decisively resolve the existence of the cellular oscillation period gradient. However, it is necessary to optimize the LuVeLu imaging protocol before proceeding to track cells in parallel. The remaining tasks for this challenge also include developing the computational pipeline to track cells, then using their tracks to extract oscillation dynamics. This task is not trivial given the large data volume to handle (~100GB/embryo), and since it needs to be optimized to the data quality we obtain. The field of image segmentation and tracking algorithms has progressed rapidly, especially with the advent of light-sheet microscopy

in developmental biology. To fully appreciate and make use of the state of the art in this field, computational expertise is vital.

To conclude, there is room for improvement in the current LuVeLu imaging protocol to reduce phototoxicity. Optimizing the protocol is necessary for further applications of the technique including single cell tracking.

4.2 Possible molecular origin of the segmentation clock oscillations

We have visualized the onset of the segmentation clock gene *Lfng* using the LuVeLu reporter in the mouse model, and assessed its tissue level dynamics in detail. From our experiments, two necessary components at the onset of segmentation clock oscillations can be deduced. First, a cue is necessary for initializing the cells to synchronously upregulate *Lfng* expression during the "pulse". Second, an instruction for a period gradient is necessary to orchestrate the evolution of traveling waves. These two components in turn would be sufficient to reproduce the emergence of traveling wave patterns that we observe. I discuss below the possible molecular mechanisms for both components.

The cue of initialization is thought to cause the "pulse" of *Lfng* expression, the first synchronous activity of the oscillatory gene. Importantly, Henning Falk showed that *Hes7*, the core clock component of oscillations of the Notch signaling pathway, is not necessary for the LuVeLu pulse to occur. The subsequent oscillations of LuVeLu were not observed in the *Hes7* KO background, confirming that *Hes7* is necessary for the cyclic expression of *Lfng*. Additionally, downregulation of Notch signaling by the gamma-secretase inhibitor DAPT, also did not suppress the "pulse". Therefore, it was hypothesized that signaling pathways other than Notch were responsible for the *Lfng* pulse. Studies in zebrafish also show that DAPT treatment does not inhibit the second to third oscillation cycle of *dlc* at 65% epiboly [Riedel-Kruse et al. (2007)], suggesting that the earliest oscillations do not require intercellular Notch signaling.

Interestingly, Henning Falk also found that the FGF signaling reporter Dusp4-T2A-3xmVenus is upregulated simultaneously as the *Lfng* "pulse" in both the mesoderm and epiblast. In contrast, the Wnt signaling reporter Axin2-T2A-3xVenus did not show such upregulation during this stage, suggesting that this initial synchronous activity is gene specific. The temporal correlation between FGF and Notch signaling during the "pulse" led us to speculate that FGF signaling could be the initializing cue. Therefore we sought to downregulate FGF signaling, to observe the effect on the LuVeLu pulse. However, FGF signaling is crucial for gastrulation, namely for the proper migration of cells away from the primitive streak after EMT [Deng et al. (1994); Yamaguchi et al. (1994); Sun et al. (1999)]. I searched for suitable conditions of pharmacological inhibition of FGF signaling, such that mesoderm formation was not compromised while FGF signaling was sufficiently downregulated. It was deemed difficult to precisely control the timing and duration of drug administration, and these experiments resulted in variable results. As an outlook, I suggest it would be beneficial to test genetic perturbations such as *fgfr1* or *fgf8/fgf4* knockout mutant lines, either in full or conditionally in the mesoderm [Naiche et al. (2011); Deng et al. (1994); Yamaguchi et al. (1994); Sun et al. (1999)].

The oscillation period gradient in the PSM is a conserved feature across several organisms, including mouse, zebrafish, medaka, chick, and snakes [Gomez et al. (2008); Shih et al. (2015); Tsiairis and Aulehla (2016); Vibe (2020)]. While the oscillation period gradient has

been acknowledged for over two decades, its control mechanism remains to be established. Intuitively, signaling gradients (e.g. FGF, Wnt, Retinoic acid) present in the PSM were speculated to be responsible for regulating oscillation period. In particular, FGF signaling has received attention as a candidate. Based on fixed stainings of embryos, it was suggested that the FGF8 gradient could be responsible for the different periodicities of segmentation clock oscillations [Vasiliauskas and Stern (2001); Ishimatsu et al. (2010)]. Recent studies using live reporters have alluded to the effect of FGF activity on the dynamics of segmentation clock oscillations [Diaz-Cuadros et al. (2020)], but exactly how the FGF gradient could be linked to oscillation dynamics is still unknown.

Our findings reveal that this feature is already present at the beginning of oscillations in mice, accounting for the gradual increase in wave number over the first six oscillation cycles. Assuming the period gradient is controlled by a similar mechanism throughout somitogenesis, and across species, I speculate that signaling gradients are also responsible in this context. Tissue patterning of the gastrulating mouse embryo has been of great interest from the viewpoint of early symmetry break and fate specification [reviewed in Tam and Loebel (2007)]. At pregastrulation stages, Wnt3 is expressed in the posterior of the embryo in the proximal epiblast and is necessary for proper primitive streak formation [Liu et al. (1999)]. Wnt3a expression is detected shortly afterwards within the streak, at late streak stages (E7.5) [Takada et al. (1994)]. *fgf8* is also expressed posteriorly at pregastrulation stages, and continues to be expressed in the primitive streak along with *fgf4*[Crossley and Martin (1995); Sun et al. (1999)]. Both Wnt and FGF pathways are likely to show graded activity in the mesoderm at the onset of the segmentation clock and are therefore good candidates for instructing the oscillation period gradient.

I pursued the idea that FGF signaling controls segmentation clock oscillation dynamics using explants from later stage embryos (E10.5), detailed in Part III. There I conclude that it is unlikely that FGF signaling directly instructs for oscillation period, but is able to do so indirectly by acting at the level of oscillation phase. With the knowledge gained at these stages, it is indeed possible that FGF signaling is responsible for orchestrating the oscillation period gradient in the gastrulating mouse embryo as well. Again, genetic perturbations of FGF signaling would be informative, in this case focusing on the outcome of oscillation period.

Part III

The effect of FGF signaling on segmentation clock dynamics

Aims of the study

In part II, I uncovered how traveling waves appear in the gastrulating mouse embryo, at the onset of segmentation clock oscillations. The phenomenological basis of the traveling waves is an underlying period gradient, with fast oscillations in the proximal (posterior) and slower oscillations in the distal (anterior) regions. This period gradient continues to exist throughout the segmentation process, but its control is not well understood. While FGF signaling is suggested to control the period of the Notch pathway oscillations, evidence is still scarce, and it is not clear how the oscillation dynamics are regulated.

In part III I address the following questions:

1. What exactly is the effect of FGF signaling on the Notch pathway oscillation dynamics?
2. What is the function and biological relevance of linking signaling gradients to oscillation dynamics?

To this end, I utilize an in vitro assay of the mouse PSM (mPSM [Lauschke et al. (2013)]) to investigate the effect of FGF signaling on the oscillation dynamics. This in vitro assay provides a platform to study the emergence of traveling waves, similar to what is seen in the gastrulating mouse embryo. The emergence of a period gradient is observed de novo in this assay, allowing us to question how FGF signaling could affect its development.

The quantitative data gained by studying the in vitro model is used to precisely model the effect of FGF signaling on oscillation dynamics. I find that FGF signaling is likely to act at the level of oscillation phase, and not period directly. I present a specific but general relationship between FGF signaling and oscillation dynamics, which implies the link could function to conserve waveform dynamics at the tissue level.

CHAPTER 5

Results

5.1 The emergence of the phase gradient in the mPSM is delayed with addition of FGF8b in culture medium

What is the effect of applying exogenous FGF8b ligand on segmentation clock dynamics? To answer this, I employed an in vitro model of somitogenesis proposed in (Lauschke et al. 2013) called the mPSM, where the tailbud of an E10.5 embryo is excised and plated on a dish with the cut face attached to the glass surface. In culture, the tissue spreads outwards, while continuing to express oscillatory activity of segmentation clock genes (Fig. 5.1A–F). I visualized and quantified Notch signaling oscillation dynamics in this in vitro assay using the LuVeLu reporter [Aulehla et al. (2008)].

In this assay, LuVeLu oscillations are initially synchronous across the tissue but become phase shifted, or wavelike over time showing a propagating pattern from the center to the periphery. This is quantified as the increase in wave number, or the span of phases seen across the central periphery axis (Fig. 5.2B). Initially, the wave number is close to 0, meaning all cells oscillate synchronously. Over the course of ~14 hours, the wave number increases until it reaches ~0.64, then starts to decrease slowly. The timing in which the wave number stops increasing coincides with the timing in which tissue begins to regress at the periphery (Fig. 5.2D). This regression recapitulates the segmentation phenomenon seen in vivo, as portrayed by the appearance of morphological boundaries and associated molecular markers [Lauschke et al. (2013)]. While the wave number stops increasing at around 16 hours in culture, the slope of the phase gradient increases monotonously over 20+ hours, indicating a consistent increase in phase difference between adjacent cells (Fig. 5.2C). The continuous increase of the slope of the phase gradient is compensated by the decrease in oscillatory field length which results in halting the increase in wave number.

Such an increase in phase gradient slope can be explained by period mismatches across the central-periphery axis. Indeed, an emerging period gradient is also observed in this assay. While the tail bud is intact and attached to the embryo, cells in this part of the PSM oscillate synchronously with a period of around 130 min [Tsiairis and Aulehla (2016)]. However, when the tissue is plated in this 2D assay, the peripheral cells slow down their oscillations compared to the central cells and reach a period of around 150 min (Fig. 5.2E). Due to this period mismatch along the central periphery axis, the peripheral cells accumulate phase delay in

comparison to central cells. This results in the impression of traveling phase waves sweeping across the tissue from the center to the periphery.

Combined, my experiments show that the emergence of this phase gradient is delayed when the mPSM is cultured with exogenous FGF8b. When cultured in 8 µg/ml FGF8b, the tissue shows oscillating dynamics of LuVeLu for 40+ hours, in comparison to around 24 hours in control (Fig. 5.3A, Movie 3). The regression of tissue at the periphery is delayed, and therefore the oscillatory field stays larger for longer (Fig. 5.3D). Concurrently, the increase in phase gradient slope is also delayed (Fig. 5.3C), and as a result, the tissue oscillates more synchronously. This is observed as a slower increase of the wave number (Fig. 5.3B).

Since the increase in phase gradient slope is directly connected to the extent of period mismatch between cells, I expected a smaller period difference between the center and periphery of the tissue in high FGF8b conditions. Indeed, I observed that the peripheral period is kept lower and hence closer to the central period for longer with higher FGF8b in the medium. By comparing with results seen when 4 µg/ml FGF8b is added to the medium, I discovered that these effects on the dynamics of LuVeLu oscillations are seen in a dose-dependent manner (Fig. 5.3B–G).

Therefore, the global addition of FGF8b to mPSMs results in the alteration of segmentation clock dynamics, well characterized by the delay in the development of traveling waves. With exogenous FGF8b, cells oscillate synchronously for longer, and therefore the phase shift between cells is kept smaller. This is expressed as a lower phase gradient slope value in the experimental conditions. Next, I checked the response in FGF signaling by assessing the expression of the downstream target Dusp4.

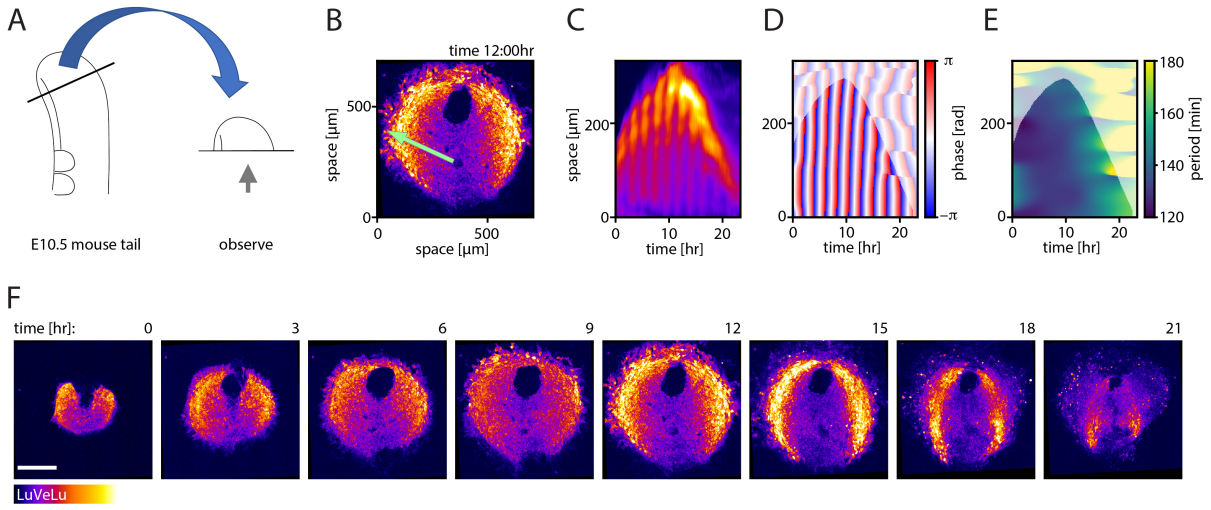

Figure 5.1: **Spatiotemporal expression dynamics of LuVeLu in the mPSM.** (A) Schematic showing mPSM method [Lauschke et al. (2013)]. The tail bud of an E10.5 mouse embryo is excised and plated on a fibronectin coated dish. (B) Still image of an mPSM sample observed from below, 12 hours from plating. The green arrow indicates the line used to generate kymograph in (C). (C) Intensity kymograph obtained by collecting intensity profiles along a line of interest over time. (D,E) Phase and period kymograph generated by processing the intensity kymograph shown in (C), respectively. (F) Still frames of a representative LuVeLu mPSM in 3 hr intervals from imaging. Note that the tissue expressing LuVeLu initially expands, but starts to regress from the peripheral regions after about 12 to 15 hours. The regression continues toward the wave center side until all tissue stops oscillating at around 24 hours in culture. scale bar: 200 µm. Experiments performed and figures made by Takehito Tomita.

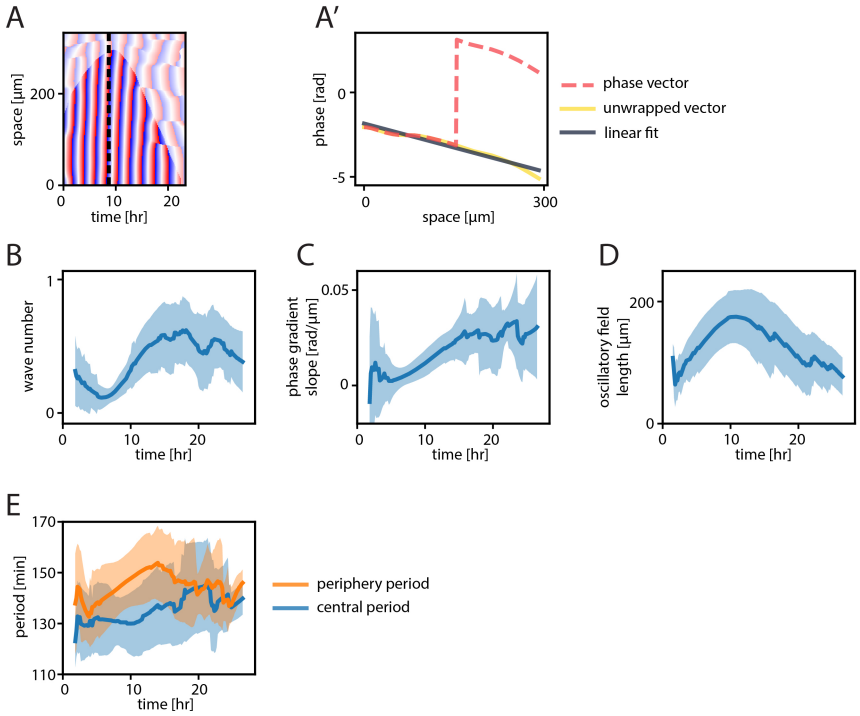

Figure 5.2: **Phase and period dynamics of LuVeLu oscillations in the mPSM.** (A) Representative phase kymograph generated from LuVeLu oscillations in an mPSM, from the sample shown in Fig. 1.1. The vertical black dashed line indicates the timepoint which is evaluated in (A'). (A') Plot showing how phase dynamics are analysed. The spatial phase gradient obtained from the kymograph in (A) at the black dashed line is represented as a red dashed line in the plot. This phase vector is first unwrapped (yellow line), then fit with a linear line (navy line). The slope is calculated from the linear fit for subsequent analyses. (B) The evolution of wave number seen in the mPSM over time, calculated by the span of phases seen in the unwrapped phase vector as exemplified in (A'). (C) The evolution of phase gradient slope seen in the mPSM over time, calculated by the linear fit to the unwrapped phase vector as exemplified in (A'). (D) The evolution of length of the oscillatory field seen in the mPSM over time. Masks generated manually using the intensity kymograph were used to determine the oscillatory length at each timepoint. (E) The evolution of central and peripheral periods seen in the mPSM over time. Periods were measured by collecting values from the period kymograph (e.g. Fig. 1.1E), at the contour paths of the central and periphery edges, shifted 5 pixels inward. (B–E) Line indicates mean, corridors mark ± 1 SD above and below the mean, respectively. Sample number [N=10, n=26]. Experiments performed and figures made by Takehito Tomita.

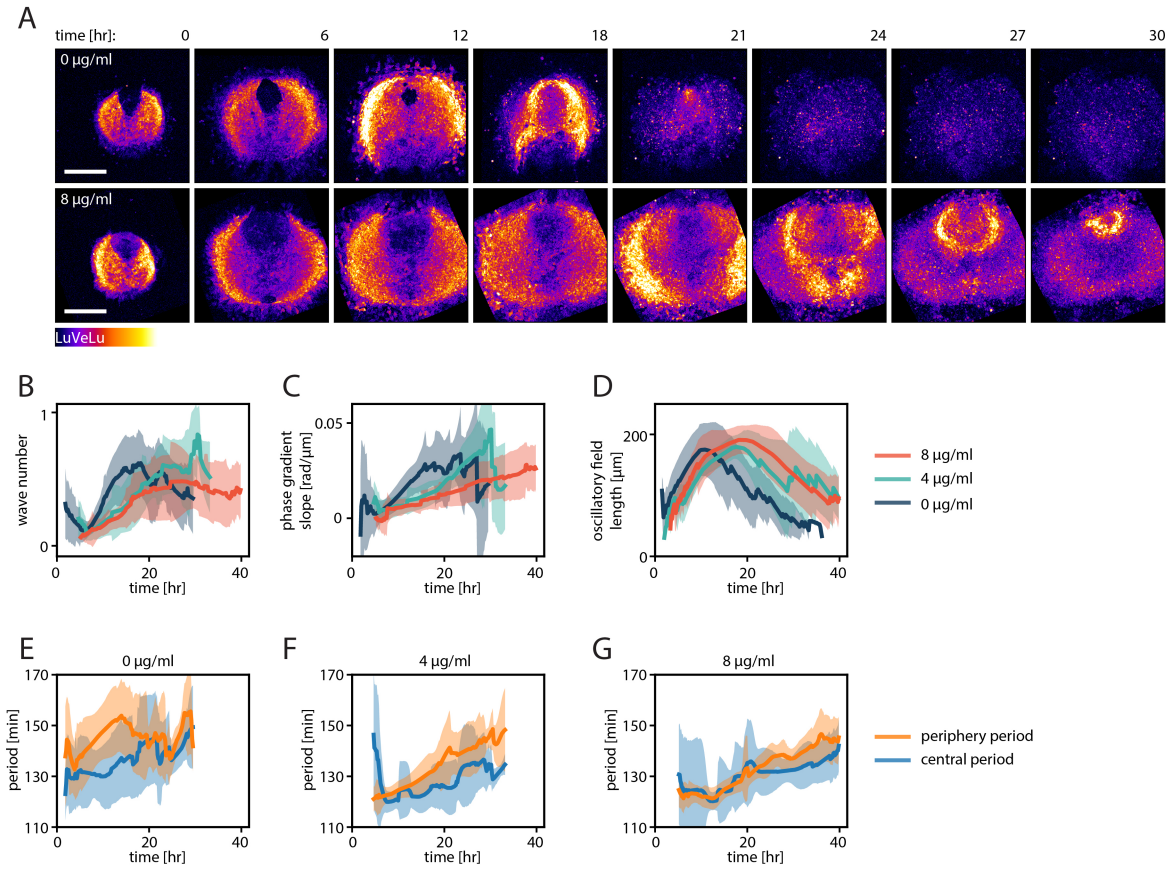

Figure 5.3: **The effect of exogenous FGF8b in medium on LuVeLu expression dynamics in mPSM samples.** (A) Still frames of a representative LuVeLu mPSM in control condition (top row) and in 8 µg/ml FGF8b (bottom row) in 6 hr intervals. Note that in the 8 µg/ml condition, the tissue the regression at the periphery does not start until around 21 hours in culture, and oscillations persist longer. scale bar: 200 µm. (B–D) Comparison of the evolution of wave number, phase gradient slope, and oscillatory field length seen in the mPSM between control (0 µg/ml), 4 µg/ml and 8 µg/ml FGF8b conditions. (E–F) Comparison of the evolution of central and peripheral periods seen in the mPSM over time, between (E) control (0 µg/ml), (F) 4 µg/ml and (G) 8 µg/ml FGF8b conditions. Note that while the central period follows a similar trajectory between the three conditions, the increase in peripheral period is delayed with higher FGF8b. (B–G) Line indicates mean, corridors mark ±1 SD above and below the mean, respectively. Sample number 0 µg/ml:[N=10, n=26], 4 µg/ml:[N=5, n=12], 8 µg/ml:[N=6, n=14]. Experiments performed and figures made by Takehito Tomita.

5.2 FGF signaling activity is still graded when cultured with exogenous FGF8b ligands or FGF signaling inhibitors

FGF signaling activity was previously shown to be graded in the mPSM in the central to periphery direction, by analysing the expression of the FGF target gene Dusp4 [Lauschke et al. (2013)]. I used the Dusp4-T2A-3xmVenus reporter line and quantified its fluorescence intensity as a proxy of FGF signaling activity in the mPSM. Confirming previous observations, mVenus intensity was indeed graded from the center to the periphery, following the direction of wave propagation. Specifically, the highest intensity was observed at the dorsal and ventral edges of the mPSM, which progressively weakened toward the left and right mesoderm tissue (Fig. 5.4A Movie 4). When the mPSMs were cultured in exogenous FGF8b ligand, the expression of Dusp4-T2A-3xmVenus was globally upregulated, while keeping the spatial expression pattern. I.e., the spatial gradient still formed in the presence of exogenous ligands (Fig. 5.4B).

Inhibition of FGF signaling also led to a persistent formation of a spatial gradient of Dusp4 activity. I cultured mPSMs in the presence of a MEK1/MEK2 inhibitor, PD0325901. FGF signaling activity is effectively reduced with this compound, as I observed that in this case, Dusp4-T2A-3xmVenus was globally downregulated. However, the spatial gradient was still present as the center still showed higher signal intensities compared to the periphery (Fig. 5.4C).

Therefore, with either global activation or inhibition of FGF signaling, the spatial gradient of Dusp4 expression persists in an upregulated or downregulated manner.

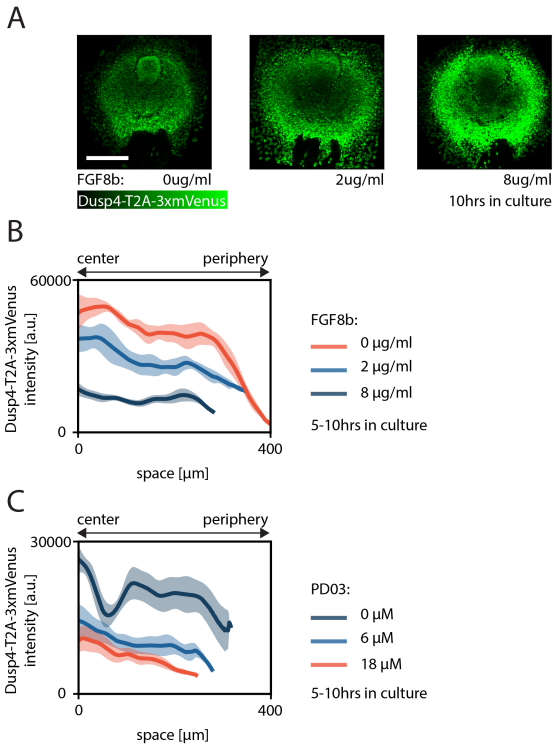

Figure 5.4: **FGF signaling activity assay in mPSMs during culture experiments** (A) Still images of mPSM samples carrying the Dusp4-T2A-3xmVenus reporter, cultured for 10 hours in conditioned medium containing 0, 2 or 8 µg/ml FGF8b ligand. scale bar: 200 µm. (B) Spatial gradient of Dusp4-T2A-3xmVenus signal during culture in 0, 2 or 8 µg/ml FGF8b ligand. Datapoints obtained during 5-10 hours in culture (30 timepoints per sample) are considered. (C) Spatial gradient of Dusp4-T2A-3xmVenus signal during culture in 0, 6 or 18 µM PD03 (FGF inhibitor). Datapoints obtained during 5-10 hours in culture (30 timepoints per sample) are considered. (B,C) Line indicates mean, corridors mark ±1 SD above and below the mean, respectively. Sample number FGF8b samples: 0 µg/ml:[N=1, n=2], 2 µg/ml:[N=1, n=2], 8 µg/ml:[N=1, n=2]. PD03 samples: 0uM:[N=1, n=2], 6uM:[N=1, n=2], 18uM:[N=1, n=1]. Experiments performed and figures made by Takehito Tomita.

5.3 8 µg/ml FGF8b loses efficacy after 48 hours in culture.

To check whether the efficacy of FGF8b is stable during culture, I reused 8 µg/ml FGF8b medium used previously for 48 hours, on a freshly prepared tailbud tissue and observed the effect on oscillation dynamics. The results showed that the reused 8 µg/ml FGF8b medium loses potency to alter LuVeLu expression dynamics, while allowing the mPSMs to survive and show dynamics equivalent to control (reused 0 µg/ml FGF8b medium). Quantification of LuVeLu expression dynamics showed that the increase in phase gradient slope overlaps with that of control samples, therefore indicating that the FGF8b ligand is either degraded or becomes ineffective over the course of 48 hours in culture (Fig. 5.5A).

This then suggests that the mPSM tissue experiences a temporally dynamic level of FGF8b when cultured with exogenous ligands. Therefore, the effects described in section 5.1 can be seen as the integral of a decaying FGF effect. Focusing on the effect of FGF8b on the phase gradient slope, it is possible that FGF levels are directly correlated with the value of the phase

gradient slope. In order to test this hypothesis, I continued to experiment with the ad hoc addition of exogenous FGF8b in a setting where the phase gradient is already established.

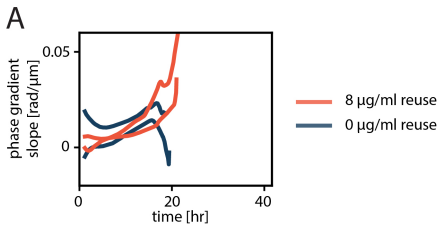

Figure 5.5: **8 µg/ml FGF8b medium does not show potency after 48 hours in culture.** (A) Comparison of the evolution of phase gradient slope seen in the mPSM between control (reused 0 µg/ml) and reused 8 µg/ml FGF8b conditions. Note that the increase is also consistent with mPSM cultured in control (0 µg/ml) condition shown in Fig. 1.3C. Sample number reused 0 µg/ml:[N=1, n=2], reused 8 µg/ml:[N=1, n=2]. Experiments performed and figures made by Takehito Tomita.

5.4 Preexisting phase gradients in the mPSM are negated with ad hoc addition of FGF8b in culture medium

To test the possibility that FGF levels directly correlate with the value of the phase gradient slope, I performed the addition of exogenous FGF8b on mPSMs where the phase gradient is already established. The results combined suggest that FGF levels are not uniquely related to values of the phase gradient slope, but rather define its rate of change. mPSMs were cultured for 16 hours in 0 µg/ml FGF8b medium, then switched to freshly prepared 0 µg/ml, 4 µg/ml or 8 µg/ml FGF8b medium. While the slope of the phase gradient continued to increase in control conditions, the slope decreased after the addition of either 4 µg/ml or 8 µg/ml FGF8b medium, meaning that the oscillations became more synchronous (Fig. 5.6A, Movie 5). For the 0 ⇒ 4 µg/ml condition, this decrease is transient, and the slope starts to increase again after about 10 hours. For the 0 ⇒ 8 µg/ml condition, this transiency is not observed during the span of the experiment (40+ hours). The regression of the oscillatory field pauses after the addition of fresh FGF8b, as seen in the representative kymographs (Fig 5.6C, D). The regression resumes in the 0 ⇒ 4 µg/ml condition but is not clearly seen to resume in the 0 ⇒ 8 µg/ml condition within 40 hours.

Although the slope of the phase gradient transiently decreases after the addition of exogenous FGF8b, it does not reach levels that are seen in the beginning of culture, where the cells are oscillating in almost complete synchronization. To see whether this can be achieved in different experimental conditions, 4 ⇒ 4 µg/ml and 8 ⇒ 8 µg/ml conditions were also tested. In the 4 ⇒ 4 µg/ml condition, the phase gradient slope decreases after the addition of freshly prepared 4 µg/ml FGF8b medium, and reaches a lower level than that of the 0 ⇒ 4 µg/ml condition (Fig. 5.6E). In the 8 ⇒ 8 µg/ml condition, the phase gradient slope is kept close to 0 at complete synchronization for over 36 hours (Fig. 5.6F). These results suggest that the value of the phase gradient slope does not directly correlate with FGF8b levels in the medium, but its increase or decrease is affected by the FGF8b level. High FGF8b levels can synchronize phase shifted oscillations exhibited by the cells, negating preexisting phase gradients.

On the other hand, removal of exogenous FGF8b allows the increase of phase shift, as seen in the 8 ⇒ 0 µg/ml condition (Fig. 5.6G). Here mPSMs were cultured in 8 µg/ml FGF8b medium for 16 hours, then changed to freshly prepared 0 µg/ml FGF8b medium. Compared to control where the mPSMs continued to be cultured in the same 8 µg/ml FGF8b medium, the slope of the phase gradient rises faster when exogenous FGF8b is removed.

To conclude, high FGF8b levels in the medium acts to synchronize *Lfng* oscillations in the mPSM, which otherwise develops phase shifts over time. When mPSMs are cultured with high FGF8b from the beginning, the development of the phase shift is delayed until the exogenous ligand loses efficacy. In cases where phase shift is already established, adding high FGF8b levels can reverse this and force the cells to oscillate more synchronously. The regression of the mPSM tissue at the periphery is correlated with the development of the phase gradient, and high FGF8b levels can delay or pause this regression.

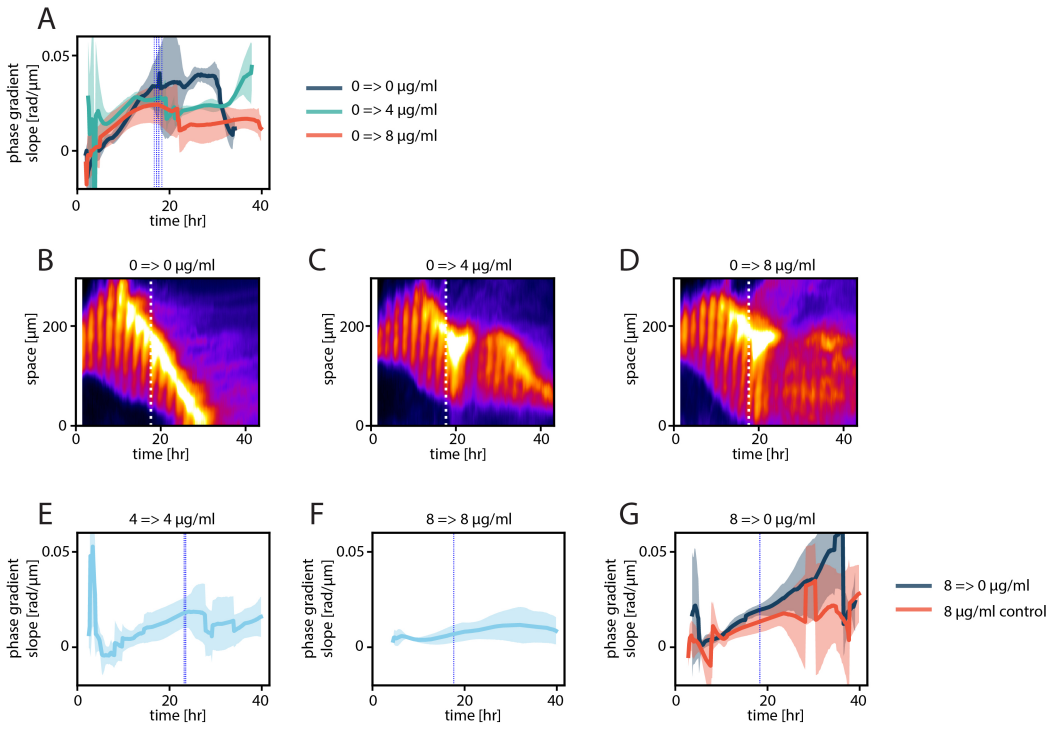

Figure 5.6: **The effects of ad hoc addition of FGF8b on the mPSM.** (A) Comparison of the evolution of phase gradient slope seen in the mPSM between control (0 ⇒ 0 µg/ml switch) and 0 ⇒ 4 µg/ml switch, 0 ⇒ 8 µg/ml switch conditions. The switch of medium was made around 16 hours in culture, as indicated by blue vertical lines in the plot. (B–D) Representative intensity kymographs of LuVeLu expression in mPSMs seen in medium switch experiments. The timing of medium change is indicated by the white dashed vertical lines. (E–G) The evolution of phase gradient slope seen in the mPSM in 4 ⇒ 4 µg/ml switch, 8 ⇒ 8 µg/ml switch and 8 ⇒ 0 µg/ml switch conditions, respectively. The switch of medium was made around 16 hours in culture in (F) and (G), and 24 hours in culture for (E), as indicated by blue vertical lines in the plots. (A,E–G) Line indicates mean, corridors mark ±1 SD above and below the mean, respectively. Sample number 0 ⇒ 0 µg/ml switch:[N=4, n=7], 0 ⇒ 4 µg/ml switch:[N=2, n=3], 0 ⇒ 8 µg/ml switch:[N=3, n=7], 4 ⇒ 4 µg/ml switch:[N=2, n=8], 8 ⇒ 8 µg/ml switch:[N=1, n=3], 8 ⇒ 0 µg/ml switch:[N=1, n=3], 8 µg/ml control:[N=1, n=6]. Experiments performed and figures made by Takehito Tomita.

5.5 Local administration of FGF8b by agarose beads on the mPSM show anisotropic synchronization effects on LuVeLu oscillations

I next tested the effects of local administration of FGF8b on the mPSMs. I modified the protocol used in [Dubrulle et al. (2001)] to prepare fluorescent heparin agarose beads soaked in either FGF8b ligand (1mg/ml FGF8b in 1%BSA/PBS) or in control solution (1%BSA/PBS). These beads were placed inside silicon wells (Ibidi micro-Insert 4 Well FulTrac) and the mPSM was placed over the bead. The tissue spread over the bead during culture, eventually covering the inside of the silicon well (Fig. 5.7A).

Interestingly, local administration of FGF8b results in a synchronization effect of LuVeLu oscillations propagated anisotropically in the direction of traveling waves. When mPSMs were cultured over FGF beads, LuVeLu oscillations were still seen to occur from the center to the periphery, and tissue regression occurred from the periphery inwards. However, I noticed that with the FGF bead, tissue regression was delayed, and the LuVeLu oscillations persisted longer compared to the contralateral side, or to when control beads were used. Interestingly, the phase gradient peripheral to the FGF bead was shallow compared to the center. I.e., cells peripheral to the FGF bead showed more synchronous oscillations. In Fig. 5.7A, oscillation phases of the LuVeLu signal are shown in the second and fourth rows, for the control bead and FGF bead sample respectively. Contour lines are drawn with spacings of 1 rad on these phase representations. Note that for the control bead sample, the contour lines gradually become dense on both sides, with or without the bead, indicating an increase in phase gradient slope. However, for the FGF8b bead sample, the contour lines peripheral to the bead stay apart for longer, while the contour lines on the contralateral side become dense over time.

Fig. 5.7B shows the evolution of the phase gradient over time for control bead samples and FGF8b bead samples. Phase profiles are obtained from the center towards the bead (red lines) or the contralateral control side (navy lines). The position of the bead is indicated by the blue vertical line in the plot. Note that the red and navy lines overlap for the control bead samples on the top row, as they both get steeper over time. However, for the FGF8b bead samples, the red line is shifted upwards compared to the navy line, peripheral to the bead position. This indicates that the oscillations peripheral to the FGF8b bead stay synchronous over time, demonstrating an anisotropic effect of the FGF8b bead.

As shown previously, FGF8b delays the emergence of the phase shift gradient in this context as well. However, the bead experiments show that this synchronization effect is propagated in the direction of the oscillation waves in an anisotropic manner. This suggested that at least partially, the effect of FGF8b on the *Lfng* oscillations is mediated through the tissue by intercellular coupling.

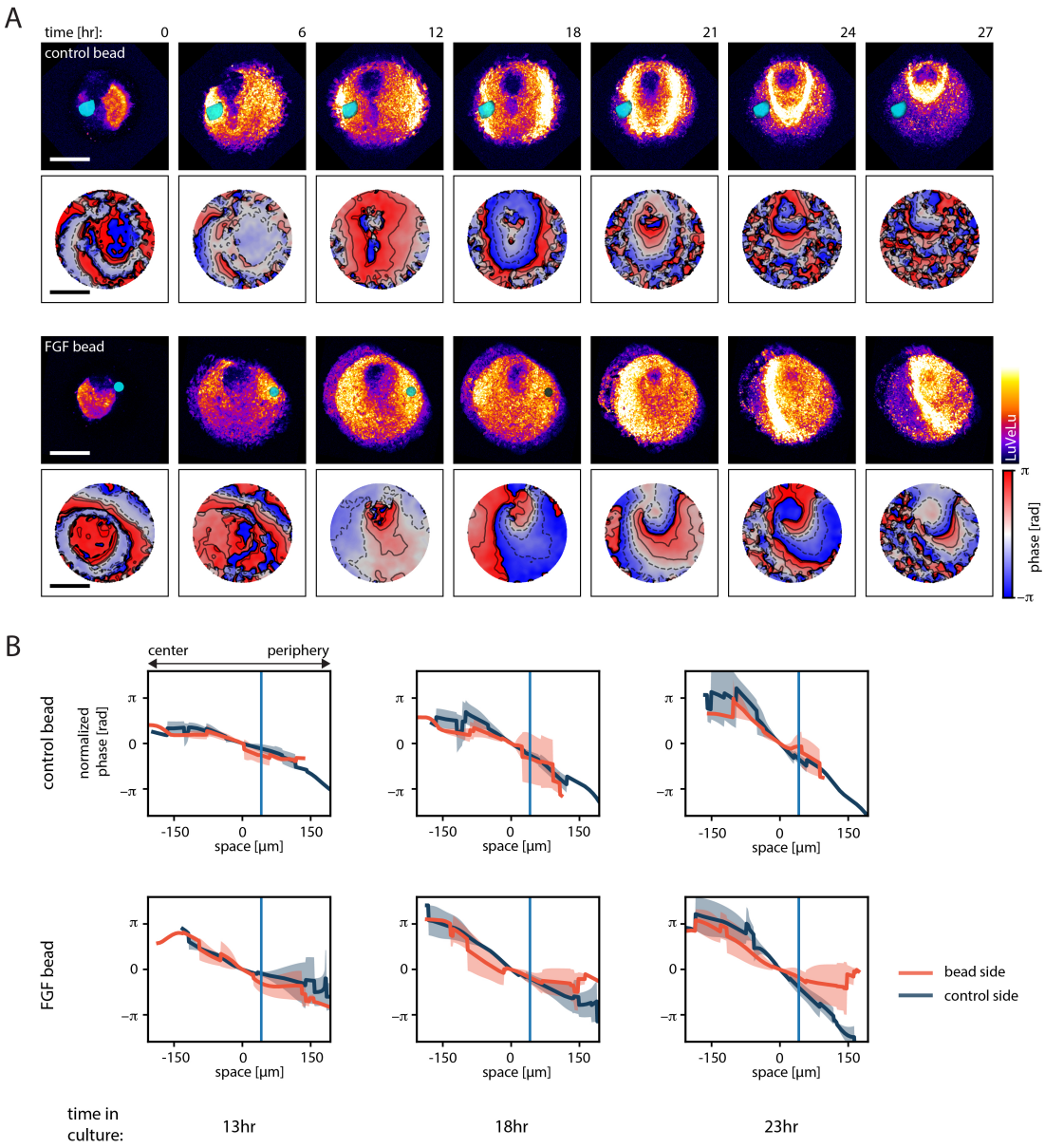

Figure 5.7: **The effects of local administration of FGF8b by agarose beads on the mPSM.** (A) Still frames of a representative LuVeLu mPSM in 6 hr intervals from imaging, either with a control bead (first row) or FGF8b bead (third row). The fluorescent signal from the bead is shown in cyan. The second and fourth rows show phase values of the oscillations seen in each sample. Contour lines are drawn on the phase representations with spacings of 1 rad. scale bar: 200 μm. (B) The evolution of phase gradient in the LuVeLu mPSM either with a control bead (top row) or FGF8b bead (bottom row). Phase gradients are measured from the wave origin in the center towards the periphery. Phase profiles were normalized at positions 30 pixels (~41μm) towards the center from the bead. This position is indicated as 0 μm in the plot. Bead positions are indicated by vertical blue lines. Note that for the control bead, the phase gradient gradually becomes steeper for both the bead side and the control side similarly. For the FGF8b bead, the phase profile periphery to the bead is shifted upwards compared to the control side. (B) Line indicates mean, corridors mark ±1 SD above and below the mean, respectively. Sample number control bead:[N=4, n=5], FGF8b bead:[N=3, n=6]. Experiments performed and figures made by Takehito Tomita.

5.6 Modeling the effect of FGF signaling on the *Lfng* oscillation dynamics in the mPSM

In [Lauschke et al. (2013)], a phenomenological model describing the *Lfng* oscillation dynamics in the mPSM was proposed. The oscillation phase at time t, position x was defined as $\phi(x,t)$, where $x = 0$ denotes the wave source. Therefore $\phi_0 = \phi(0,t)$ represents the oscillation phase at the wave source. The phase difference between the wave source and position x at time t is then defined as $\Delta\phi(x,t) = \phi(0,t) - \phi(x,t)$. The model postulates that the phase difference $\Delta\phi$ follows an exponential law in time, or

$$\frac{\partial\Delta\phi}{\partial t} = \alpha\Delta\phi \tag{5.1}$$

It also assumed that the phase shift gradient in space was linear, or

$$\Delta\phi(x,t) = \Gamma x \tag{5.2}$$

A model that satisfies (2.1) and (2.2) was

$$\Delta\phi(x,t) = \lambda e^{\alpha t}x \tag{5.3}$$

Where λ is a length scale parameter set to $3.0 \cdot 10^{-3}$. This phenomenological model is hereinafter referred to as the static α model. Here the slope of the phase gradient, $\Gamma = \lambda e^{\alpha t}$ increases exponentially over time as well. I focus on this value as this is a relatively reliable measurement to extract from the data. Fig. 5.3C shows that with the addition of exogenous FGF8b ligand, the temporal evolution of the slope is affected. An intuitive way to interpret this result in the framework of the model is to change the value of α. Indeed, by decreasing the α parameter, the function $\lambda e^{\alpha t}$ can be fit to conditions with higher concentrations of FGF8b ligand (Fig. 5.8A,B).

However, simply associating the concentration of exogenous FGF8b ligand to a value of α does not explain the results of ad hoc addition of FGF8b. Here, mPSMs were cultured for 16 hours, and FGF8b ligand was added to the medium. In this case, the slope of the phase gradient decreased after the addition of FGF8b ligand. If for instance, 8 µg/ml FGF8b was associated with an α value of $9.40 \cdot 10^{-4}$, one would expect that with medium change, the slope would continue to increase, although more slowly. In order to have the slope decrease, the α value needs to be negative. It also cannot continue to be negative, as we observe that eventually, the slope starts to increase again. Therefore, to accommodate all the experimental results within the framework of the model, the α value needs to change dynamically over time. The revised model, where α depends on time, will be referred to as the dynamic α model, and satisfies the following relationship:

$$\frac{\partial\Delta\phi}{\partial t} = \alpha(t)\Delta\phi \tag{5.4}$$

I showed that FGF8b ligand loses efficacy after 48 hours in culture (Fig. 5.5A). From this data I can assume that FGF8b ligand added in culture medium gradually loses its effect over time, which can be translated to changing values of α. Although $\alpha(t)$ can be determined freely, I assumed it to exponentially converge to the "natural" α value $\alpha_0 = 2.10 \cdot 10^{-3}$, when deviated from it. Therefore,

$$\alpha(t) = \alpha_0 - (\alpha_0 - \alpha_1)e^{\beta t} \quad (\beta < 0) \tag{5.5}$$

At time $t = 0$, $\alpha(t) = \alpha_1$, and at $t = \infty$ converges to α_0, with its speed depending on the value of β. Based on this function, I searched within a parameter space to obtain the following set:

parameter	value
λ	$3.0 \cdot 10^{-3}$
α_0	$2.10 \cdot 10^{-3}$
4 µg/ml α_1	$-1.44 \cdot 10^{-3}$
8 µg/ml α_1	$-3.66 \cdot 10^{-3}$
β	$-2.80 \cdot 10^{-3}$

These parameters were used to generate simulations of phase gradient slope values for the various experimental schemes including the ad hoc FGF8b addition experiments (Fig. 5.8C–L). Using this new framework, it was possible to qualitatively capture the movement of slope values. Importantly, slopes are simulated to decrease after the ad hoc addition of FGF8b (Fig 5.8E–J), while they only slowly rise when FGF8b is added to medium from the beginning (Fig 5.8C,D). However, there are still quantitative discrepancies, and it would be necessary to consider different functions to simulate the temporal change in $\alpha(t)$.

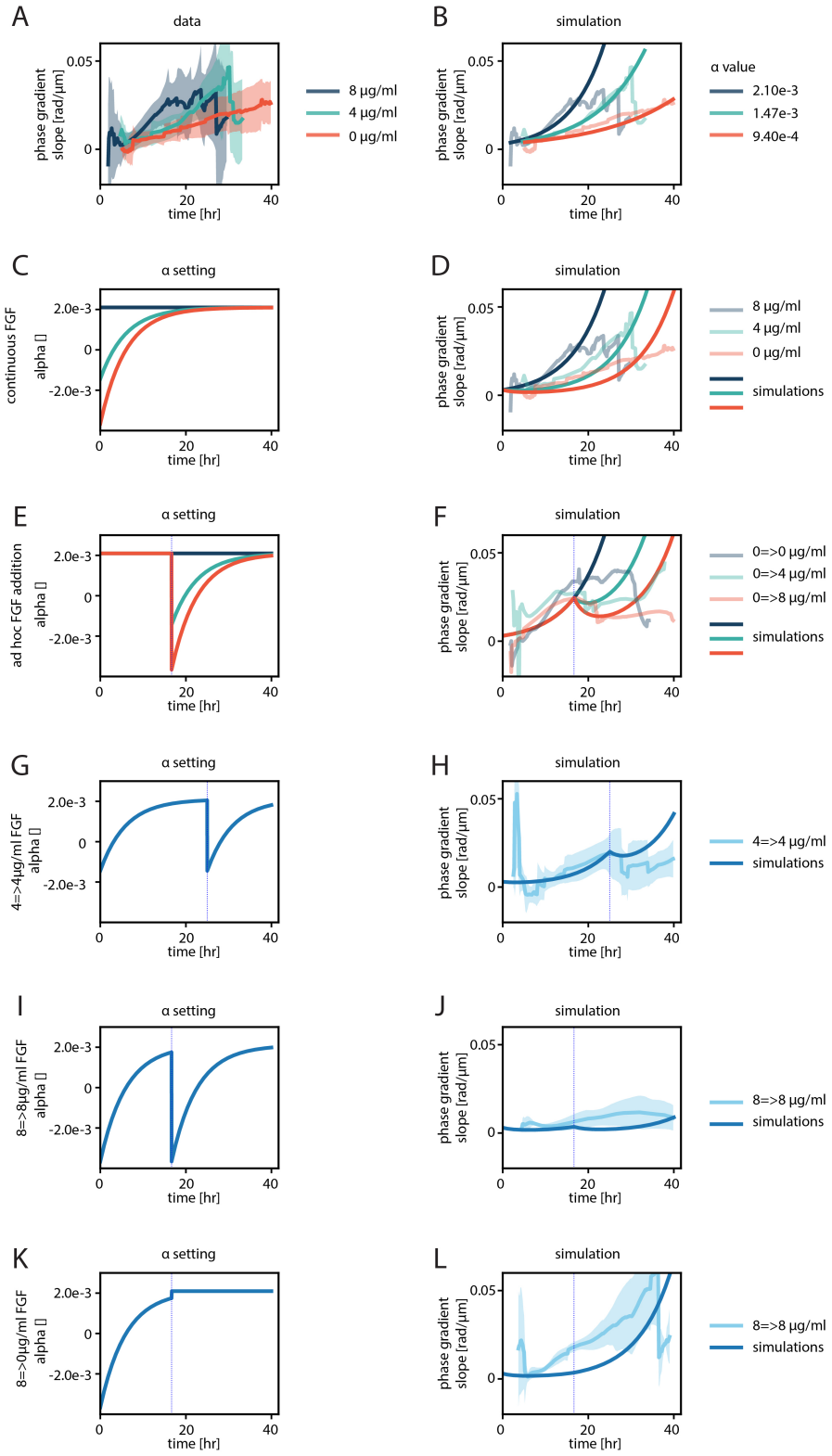

Figure 5.8: **Simulations of the phase gradient slope based on the α model.** (A) (Identical to Fig.1.3C) Comparison of the evolution of phase gradient slope seen in the mPSM between control (0 μg/ml), 4 μg/ml and 8 μg/ml FGF8b conditions. (B) Simulation of the evolution of phase gradient slope based on the static α model: slope $= \lambda e^{\alpha t}$. (C–L) Simulation of the evolution of phase gradient slope based on the dynamic α model: $\frac{\partial \Delta\phi}{\partial t} = \alpha(t)\Delta\phi$. $\alpha(t)$ settings for each simulation is shown on the left column plots, and the corresponding simulations are shown in the right column plots, with the experimental results overlaid. (A,B,D,F,H,J,L) Line for experimental data indicates mean, corridors mark ± 1 SD above and below the mean, respectively. Simulations performed and figures made by Takehito Tomita.

5.7 Extrapolations from the dynamic α model

The dynamic α model makes intriguing predictions about the frequencies of the oscillations which should be observed. The model is agnostic about the basal frequency of the system, as it only defines the phase relationship between oscillators at different positions. Nevertheless we can describe the oscillator frequency at $x = 0$ as $\omega(0,t) = \frac{\partial\phi(0,t)}{\partial t}$. It follows that the frequencies of the oscillations in other positions can be described in terms of $\omega(0,t)$:

$$\phi(x,t) = \phi(0,t) - \Delta\phi(x,t) \tag{5.6}$$

$$\omega(x,t) = \frac{\partial\phi(x,t)}{\partial t} = \omega(0,t) - \frac{\partial\Delta\phi(x,t)}{\partial t} \tag{5.7}$$

In the dynamic α model, I define $\frac{\partial\Delta\phi(x,t)}{\partial t} = \alpha(t)\Delta\phi(x,t)$. Therefore,

$$\omega(x,t) = \omega(0,t) - \alpha(t)\Delta\phi(x,t) \tag{5.8}$$

Because the waves are always traveling from the center ($x = 0$) to the periphery ($x > 0$), and therefore the oscillations at the periphery are phase delayed, $\Delta\phi(x,t) > 0$. In the dynamic α model, $\alpha(t)$ can take negative values. In fact, this property was necessary to capture the decrease in phase gradient slope we observe in the ad hoc FGF8b addition experiments. When $\alpha(t) < 0$, since $\Delta\phi(x,t) > 0$, $\omega(x,t) > \omega(0,t)$. This means that the oscillators at the periphery of the mPSM oscillate faster than the center. This phenomenon occurs when the phase difference between oscillators is decreasing, or in other words, the peripheral oscillators are catching up to the central oscillators. It is therefore intuitive that during that time, the peripheral oscillators must be running faster than the central oscillators.

This extrapolation is intriguing since the mPSMs recapitulate the anterior-posterior axis of the intact PSM along the central periphery axis [Lauschke et al. (2013)]. It is shown that there also exists a frequency gradient in the anterior-posterior axis of the intact PSM, with the fastest oscillations in the posterior and slower oscillations in the anterior in mice and zebrafish [Giudicelli et al. (2007); Tsiairis and Aulehla (2016); Shih et al. (2015)]. It has been suggested that FGF or Wnt signaling controls the Notch signaling oscillation frequencies, as they also exhibit anterior-posterior gradients in the PSM. In the mPSM, we also observe that FGF and Wnt activity gradients form along the central periphery axis [Lauschke et al. (2013)], and the frequency gradient has always corresponded to this axis. However, the results we obtained in the ad hoc FGF8b addition experiments indicate that this relationship could be decoupled; i.e., peripheral oscillations can run faster than the central oscillations, with presumably less FGF8b ligand. This suggests that FGF8b ligand levels do not correlate with oscillation frequency directly.

In future studies, it is crucial to measure FGF signaling activity in the ad hoc FGF8b addition experiments by using reporter lines of Dusp4 and others. It is also crucial to extend the experiments using intact PSM tissue, to see if similar results are obtained. How the frequency gradient is regulated in the intact PSM is still unknown, but my results suggest that FGF signaling affects oscillations at the level of oscillation phase. It is possible that these effects are translated into the level of frequency to manifest as a frequency gradient. Further investigation especially with intact PSM is necessary to confirm this hypothesis.

5.8 Anisotropic effect of local FGF administration on the LuVeLu oscillations

In section 5.5 I showed the effects of local administration of FGF8b on the mPSMs. I unexpectedly found an anisotropic effect of FGF8b on the LuVeLu oscillations, where local oscillations peripheral to the FGF8b bead became more synchronized. This prompted me to speculate on previously reported results. In [Dubrulle et al. (2001)], the authors reported anisotropic effects of grafting FGF8 beads in chick PSM. They showed that somites formed anterior to the FGF8 bead were smaller than control, while those posterior to it were not affected.

In short, they propose two explanations; 1. exogenous FGF8 is perceived differently at anterior and posterior positions since the endogenous FGF gradient could be shaped differently and therefore the deviation from it is different. 2. FGF8 ligand diffusion may be different at different positions, and in particular diffusion at the anterior PSM may be inhibited, therefore unable to affect somite formation at the posterior when the bead resides near the S-1 level.

My experiment adds another possible explanation to this phenomenon, which is that the segmentation clock oscillations are affected anisotropically which translates into the anisotropic effect of somite formation. The link between the segmentation clock dynamics and morphological boundary formation has been shown in [Lauschke et al. (2013); Sonnen et al. (2018)] where phase gradient slope of the LuVeLu oscillations correlated with segment size in the mPSM. In more detail, it was proposed that segment boundaries form at the position of 2π phase shift from the posterior most oscillator. This model can be extended to the intact PSM, and by including the anisotropic effect on the segmentation clock, can recapitulate the anisotropic effects on somite formation.

The effect I see on the phase gradient with FGF8b can be considered as an acceleration of wave velocity. Local wave velocity can be calculated by $v = \frac{\partial\phi}{\partial t} / \frac{\partial\phi}{\partial x}$, where $\frac{\partial\phi}{\partial t}$ is the local frequency, and $\frac{\partial\phi}{\partial x}$ the slope of the phase gradient. Decreasing the denominator, the slope of the phase gradient increases wave velocity. Based on this understanding, I made a simplified model of oscillation phase wave dynamics in the intact PSM simulating wave velocity (Fig. 5.9A). A pulse is emitted from the posterior tip with velocity v_0, and slows down with exponential kinetics: $v(t) = v_0 + 1 - e^{at}$ (Fig. 5.9B, navy line). This pulse is repeated at a period of T, while the posterior grows at a rate of g. A somite boundary is placed when the next pulse is emitted, at the position where the previous pulse reached during time T. This ensures that there is one wave spanning the PSM at any time, and therefore the observed wave number is 2π. Without perturbation, somite boundaries will be placed with a spacing of $T \cdot g$ in this model.

Assuming that an FGF bead would accelerate the wave only after it passes the bead, I can mimic this effect by increasing the wave velocity at a particular position (Fig. 5.9B, red dashed line). I allowed the velocity to increase to v_0 when it reaches the bead, and then to decrease again with the same kinetics. The resulting pattern of segmentation captures key features of the phenotype seen in [Dubrulle et al. (2001)]. That is, segment boundaries are shifted rostrally in the anterior of the bead, while the region posterior to it remains unaffected (Fig. 5.9E). Interestingly, in the simulation, the somites made just anterior of the "bead" are large compared to control. [Dubrulle et al. (2001)] also reports that "caudally to the grafted bead, a large somite formed". The position at which the large somite forms is slightly different (rostral to the bead in the simulation, and caudal to it in [Dubrulle et al. (2001)]), but this could be

adjusted in the simulation if the effect of the bead was made to extend in a locally diffusive manner.

These simulations show that the anisotropic effects of FGF signaling on segment patterning shown in [Dubrulle et al. (2001)] can be recapitulated based on changes in oscillation dynamics. It is of great interest to experiment similarly with intact mouse PSM, with FGF bead implantation to see whether predicted changes in wave velocity and patterning are observed.

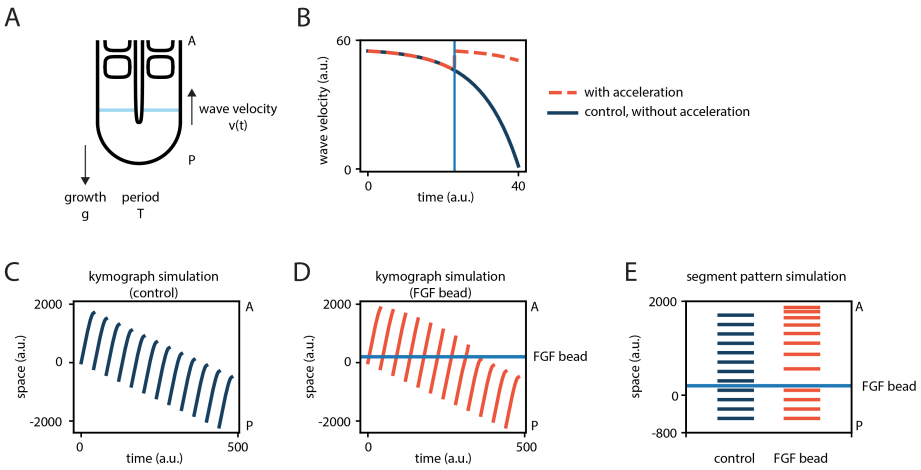

Figure 5.9: **Simulations of the segmentation patterns based on the wave velocity model.** (A) Schematic showing the components of the model. The tissue grows at a constant rate g, while pulses are emitted from the posterior tip with period T. These pulses travel in the tissue in the anterior direction with velocity $v(t)$. (B) Plot showing the dynamics of the wave velocity $v(t)$. Without perturbation, the velocity decreases with the kinetics: $v(t) = v_0 + 1 - e^{at}$ (navy solid line). The wave can be accelerated to v_0 when it reaches the "FGF bead", depicted as the blue vertical line, which then decreases again with the same kinetics afterward (red dashed line). (C) The simulation of waves in a control situation is shown as a kymograph. (D) The simulation of waves in which the FGF bead implantation was modeled. The acceleration of waves is modeled to occur at 200(a.u.) in space, depicted as the horizontal blue line. (E) Simulated segment patterns based on the wave velocity model. On the left side the control pattern is shown with navy lines, showing spacings of $T \cdot g = 200$(a.u.). On the right side, the segment pattern for accelerated waves is shown with red lines. The anterior segment boundaries are pushed anteriorly, and smaller segments are seen. The somite encompassing the "FGF bead" is larger than the control, as also the two somites anterior to it. Parameters: $g = 5$, $T = 40$, $v_0 = 55$, $a = 0.1$, bead position $= 200$. Simulations performed and figures made by Takehito Tomita.

CHAPTER 6

Discussions

6.1 FGF signaling activity gradient in the mPSM

In section 5.2 I showed FGF signaling activity reported by the Dusp4-T2A-3xmVenus signal in the mPSM when cultured with exogenous FGF8b ligand or the FGF inhibitor PD0325901. While it is unknown how well the FGF8b ligand or drug penetrates into the tissue culture, the result is that FGF signaling activity continues to be graded in both cases. It was shown in [Lauschke et al. (2013)] that the endogenous FGF8 expression is restricted to central domains of the mPSM. The endogenous concentration of FGF8b in the caudal fragment of the mouse PSM is estimated to be on the order of 0.5µg/ml [Dubrulle and Pourquié (2004)]. Since the concentration of exogenous FGF8b ligand provided in the experiments is 10-fold larger, I first expected that FGF signaling activity in the mPSM would saturate. However this was not the case, and I present here several possible explanations for this result.

The simplest hypothesis is that the exogenous ligands or drugs linearly contribute on top of the baseline FGF signaling activity in the mPSM. FGF signaling activity would be upregulated or downregulated similarly at all positions, translating the gradient up or down. Another possibility is that there are FGF receptor gradients in the mPSM. If the receptor is graded, Dusp4 activity will be graded even when ligand concentration is flat across the tissue. This hypothesis does not account for the inhibition experiments, since the drug PD03 acts on MEK1/2, downstream of the receptor. The third possibility is positive feedback of FGF signaling. [Dubrulle et al. (2001)] showed that exogenous FGF8 signaling induces ectopic FGF8 mRNA expression in chick PSM. This autocrine property of FGF could amplify signals in a positive feedback loop, ensuring that the gradient persists when additionally activated or downregulated.

The result I obtained could be due to any of the above mechanisms, or of them combined. It is still unclear exactly how the mPSMs generate a central to periphery FGF signaling gradient endogenously, but these experiments provide a lead to this problem. Quantifying the expression of FGF receptors in the tissue, as well as checking FGF8 expression in these experiments would be key.

6.2 Deducing the function of the FGF gradient on the segmentation clock dynamics

I have shown that FGF signaling affects the segmentation clock oscillations which is well characterized at the level of phase rather than period. In a phenomenological sense, exogenous FGF signal has the ability to spatially synchronize *Lfng* oscillations, preventing the evolution of phase shift between cells. From these results, what can be deduced about the function of the endogenous FGF gradient seen in the PSM? How can it be described?

First I discuss in detail the implied biological meanings of changing α in the alpha model presented earlier. In the context of the alpha model, I have suggested that the effect of exogenous FGF signal can be captured by a change in the α parameter. Understanding the model in detail leads to a biological interpretation of the results.

The core of the alpha model is based on the description that cells slow down their oscillations over time with the following kinetics:

$$\frac{\partial \Delta\phi}{\partial t} = \alpha \Delta\phi \tag{6.1}$$

In [Lauschke et al. (2013)] $\Delta\phi$ is described as the phase difference between an oscillator (e.g. cell) and the fastest oscillation in the system (at the center of the mPSM, or the tailbud of the intact PSM.) While this is acceptable as an assumption, it is not clear how cells would be able to sense the phase of oscillations occurring far away in a tissue, to calculate the phase difference against its own. To explain this, a second molecular oscillator can be introduced. If this second oscillator is always synchronized to the fastest oscillation in the system, and its activity is propagated across the tissue instantaneously, then the phase difference between the first and second oscillator in each cell can be used as $\Delta\phi$. Such a hypothesis was presented in [Sonnen et al. (2018)] , which showed that the phase difference between Notch and Wnt oscillations are functionally relevant for segment patterning.

This is a realisation of the phase shift model proposed in [Goodwin and Cohen (1969)]. The model originally postulated two waves emitted from a source, a fast S wave, and a slow P wave. The time difference between the arrival of the S wave and the P wave encodes the distance from the wave source, thereby translating temporal information to a spatial one.

Incidentally, the introduction of the second oscillator allows this model to be taken out of the tissue context, to be thought of as a cell autonomous model. The phase difference between the two molecular oscillators can be calculated regardless of the activity outside, and it can be said to follow the kinetics in equation (6.1). What the model then describes is how the phase difference between the two oscillators increases (or decreases) exponentially over time. Given our findings, FGF can be described to set the α in each cell. That is, FGF signaling activity in each cell correlates with how the two oscillators change their phase difference. High FGF activity can be related to low values of α, which ensures that the phases of the two oscillators do not drift apart. The FGF gradient found in the PSM can then encode for a graded α along the AP axis.

This understanding is slightly different from what has been previously discussed in the manuscript. I have described α, not as a cellular parameter, but more of a global one, being applied to all the cells equally. Why is such a modification necessary? The basis of it is the fact that a temporally dynamic α was necessary to explain the ad hoc FGF addition

experiments. This result, along with the fact that exogenous FGF loses efficacy over time, suggests that the α value reflects the immediate level of FGF signaling activity. Therefore, given a spatial FGF gradient, it is intuitive to postulate a corresponding α gradient.

What function does a graded α have on the resulting oscillations? Interestingly, it is not necessary for α to be graded to capture important features such as traveling waves and the period gradient. This feature can be built in the structure that the temporal derivative of $\Delta\phi$ scales to itself, under the condition that $\Delta\phi$ is graded across space from the beginning. If this is the case, spatial phase gradient is amplified over time as below (if $\alpha > 0$). Given positions x_1 and x_2,

$$\begin{aligned} \Delta\phi(x_1) &< \Delta\phi(x_2) \\ \alpha\Delta\phi(x_1) &< \alpha\Delta\phi(x_2) \\ \frac{\partial\Delta\phi(x_1)}{\partial t} &< \frac{\partial\Delta\phi(x_2)}{\partial t} \end{aligned}$$

therefore, $\Delta\phi(x_2)$ increases faster compared to $\Delta\phi(x_1)$, amplifying their difference. With ϕ_0 as the phase of the second intracellular oscillator synchronized across space, it also follows that

$$\begin{aligned} \frac{\partial(\phi_0 - \Delta\phi(x_1))}{\partial t} &> \frac{\partial(\phi_0 - \Delta\phi(x_2))}{\partial t} \\ \omega(x_1) &> \omega(x_2) \end{aligned}$$

Therefore allowing a frequency (period) gradient to emerge between the positions.

However, it is crucial that $\Delta\phi$ is graded properly as an initial condition. If there is no $\Delta\phi$ gradient from the beginning, symmetry break cannot occur, and oscillations would simply ensue in synchrony. A graded α can solve this issue by providing another source of spatial asymmetry. In this case, even when there is no gradient of $\Delta\phi$, the difference in alpha would force it to emerge.

$$\begin{aligned} \alpha(x_1) &< \alpha(x_2) \\ \alpha(x_1)\Delta\phi &< \alpha(x_2)\Delta\phi \\ \frac{\partial\Delta\phi(x_1)}{\partial t} &< \frac{\partial\Delta\phi(x_2)}{\partial t} \end{aligned}$$

Therefore a graded α ensures that traveling waves occur in the direction from low to high α. In addition, a frequency gradient also emerges following the same line of logic stated above. This function may be important especially at the onset of the segmentation clock oscillations. I have shown in section 3.2 that traveling waves emerge as a gradual build up, with a small phase gradient in the beginning. Since the $\Delta\phi$ gradient is small in the beginning, noise can easily lead to unfavourable outcomes, such as multiple nucleation sources of traveling waves.

A graded α would be a feature to prevent such cases, increasing reproducibility and robustness of the oscillation dynamics.

Interestingly, FGF4 and FGF8 double knockout mutant in the mesoderm leads to multiple somite-like structures disorganized with abnormal segmentation planes [Naiche et al. (2011)]. It is proposed that these structures form in a single wave of differentiation rather than sequentially. Mesoderm is rapidly used up at late headfold stages of the embryo (E8.0), followed by axial truncation. This phenotype hints a connection with "Somites Without a Clock" [Dias et al. (2014)]. Here posterior primitive streak explants from quail or chick were dorsalized by applying the BMP antagonist Noggin, and grafted into the extraembryonic region of a host chick embryo. After 9-12 hours, 6-14 somite-like structures appear, "arranged as a bunch of grapes." There is presumably no spatial FGF gradient in both these cases, and this could indeed represent a case where AP axis instruction is lost. It is tempting to speculate that multiple nucleation sources of traveling waves appear in these settings, leading to simultaneous construction of somite-like structures. A suggestive case is observed when PSM cells are dissociated, randomized and reaggregated, then plated on a glass surface [Tsiairis and Aulehla (2016)]. These cells resynchronize their oscillatory gene expression with their neighbours and create multiple foci showing concentric waves. Each focus acts like an mPSM, and at the periphery of each focus, *Mesp2*, a molecular marker for segmentation initiation, is upregulated after oscillation arrest. These foci appear at characteristic length scales and self-organise a pattern not unlike a "bunch of grapes" in 2D. Such a process could be occurring in cases without an FGF gradient. As we are equipped to image segmentation clock oscillations at the gastrulating mouse embryo, imaging the LuVeLu signal in the mesoderm FGF4/FGF8 KO line would be an informative loss of function experiment of the FGF gradient.

It is important to point out the difference between the hypothesis that FGF signaling activity controls α and the hypothesis that FGF signaling activity controls oscillation frequency [Ishimatsu et al. (2010)]. At least in the mouse model, the latter is unlikely due to the results seen in the ad hoc FGF addition experiments, detailed in sections 5.4 and 5.7. In short, FGF8b ligand levels do not seem to correlate with LuVeLu oscillation frequencies in these experiments. Instead, allowing FGF signaling to define the α parameter captures the outcome well. In this unique experimental setting, we are thus able to differentiate the two hypotheses. However, in physiological conditions, a gradient of α usually results in the period gradient appearing in the same orientation. A graded α essentially gives instruction for polarity and can be understood to connect the orientation of the signaling gradient to polarities in oscillation dynamics, such as the direction of traveling waves and the orientation of the period gradient.

To conclude, I propose that FGF signaling in the mouse PSM acts to determine how oscillation phase shift evolves. This is both in the sense of spatial phase shift measured in Notch signaling oscillations, and in the context of the two oscillator model, intracellular phase shift between the two oscillators. Specifically, the idea that FGF governs the relationship between Notch and Wnt oscillations is an attractive hypothesis linking the three pathways. Recent studies have supported this novel function of FGF signaling regulating the dynamics of oscillatory genes [Diaz-Cuadros et al. (2020)], and my results shed light on how exactly they may be linked. Based on this framework, future experiments can be designed to challenge the model in different contexts, including ex vivo settings of the gastrulating mouse embryo and intact PSM at E10.5 stages, as well as in other species.

6.3 FGF signaling as the link between oscillation dynamics and cellular movement

The significance of connecting FGF signaling activity to oscillation dynamics can be observed from a slightly different perspective. We start with the continuum mechanics approach presented in [Giudicelli et al. (2007); Gomez et al. (2008); Morelli et al. (2009); Niwa et al. (2011)]. I postulate a cell to move around in a scalar field $\phi(x,t)$, where ϕ would be the phase of the oscillator at position x, time t. Given the velocity of the cell v in the x dimension, the frequency of this cell can be written as the material derivative:

$$\begin{aligned}\frac{D\phi}{Dt} &= \frac{\partial\phi}{\partial t} + v\cdot\nabla\phi \\ &= \frac{\partial\phi}{\partial t} + v\frac{\partial\phi}{\partial x}\end{aligned}$$

The frame of reference is taken such that the posterior tailbud of the PSM is always positioned at $x=0$. We assume that at steady-state waveforms are repeated in the PSM with a rate corresponding to the segmentation pace, or the frequency of the tailbud oscillations. In such a case, $\frac{\partial\phi}{\partial t}=\omega_0$ with ω_0 as the frequency of the tailbud oscillations. Then the intracellular frequency can be written as:

$$\frac{D\phi}{Dt} = \omega_0 + v\frac{\partial\phi}{\partial x}$$

In addition, I can assert the condition of the alpha model onto the oscillator. The phase of this particular oscillator θ can be defined in relation to the tailbud oscillator phase $\phi(0,t)$ as:

$$\theta = \phi(0,t) - \Delta\theta$$

From the alpha model:

$$\frac{\partial\Delta\theta}{\partial t} = \alpha\Delta\theta$$

Therefore the intracellular frequency of this oscillator can be defined as:

$$\begin{aligned}\frac{\partial\theta}{\partial t} &= \omega_0 - \frac{\partial\Delta\theta}{\partial t} \\ &= \omega_0 - \alpha\Delta\theta\end{aligned}$$

Given this oscillator moves with velocity v, it holds that $\frac{D\phi}{Dt}=\frac{\partial\theta}{\partial t}$, as they are both definitions of intracellular frequency. From this I derive the condition:

$$v\frac{\partial\phi}{\partial x} = -\alpha\Delta\theta \tag{6.2}$$

This relates the cellular velocity v, the spatial phase gradient $\frac{\partial\phi}{\partial x}$, the oscillation dynamics parameter α, and the intracellular phase delay $\Delta\theta$. Given a particular shape of the phase gradient the system needs to achieve, which is invariant across time, noted $\Delta\theta(x)$, ϕ can be written as

$$\phi(x,t) = \phi(0,t) - \Delta\theta(x)$$

and therefore

$$\frac{\partial\phi}{\partial x} = -\frac{\partial\Delta\theta(x)}{\partial x}$$

Inserting this into equation (7.2), I obtain

$$v\frac{\partial\Delta\theta(x)}{\partial x} = \alpha\Delta\theta(x) \tag{6.3}$$

Therefore, the shape of the phase gradient constrains the relationship between the cellular velocity v and the dynamics parameter α. Equation (7.3) can be written as:

$$\alpha = v\frac{\partial\ln(\Delta\theta(x))}{\partial x} \tag{6.4}$$

Note that when $\Delta\theta(x)$ takes an exponential form $Ae^{\beta x}$, $\alpha = v\beta$ and the two quantities α and v are proportional. If $\Delta\theta(x)$ is linear or quadratic, $\alpha \propto v/x$.

The cellular velocity v has been defined differently by different groups. In [Morelli et al. (2009); Niwa et al. (2011)], it is assumed to be a constant independent of position. In [Giudicelli et al. (2007); Gomez et al. (2008)], velocity is assumed to linearly correlate with position; $v = 0$ at the posterior tailbud, increasing to $v =$somite size/segmentation period in the anterior most PSM. Experimental data in chick and quail suggest that cellular velocity in the AP axis is graded in the PSM [Bénazéraf et al. (2010, 2017)]. These studies take the anterior somite as reference, measuring the highest velocity at the posterior tailbud which decreases towards the anterior. If the posterior tailbud is taken as reference, this velocity gradient is reversed, with the highest velocity in the anterior PSM. Assuming such a velocity gradient exists, if $\Delta\theta(x)$ takes an exponential form, then $\alpha = v(x)\beta$, necessitating a graded α, such as discussed in section 6.2.

The significance of this relationship is that it highlights the potential role of FGF signaling in linking the two quantities, α and v. It has been shown that the FGF gradient is responsible for a cellular motility gradient in the chick PSM [Delfini et al. (2005); Bénazéraf et al. (2010)], which in turn controls tissue elongation. It can be speculated that the cellular velocity gradient manifests as a result of this motility gradient controlled by FGF. If FGF signaling also controls oscillation dynamics, in particular the parameter α, it can act as a link to satisfy the necessary condition stated above, to produce particular waveform shapes. It would be key to study cell velocity in the mouse PSM, its relation to FGF signaling, and to oscillation dynamics, using novel techniques enabling single cell dynamics analysis [Yoshioka-Kobayashi et al. (2020)].

6.4 Reconciliation with the clock and wavefront model

Throughout the manuscript, I have discussed a novel function of FGF signaling on the segmentation clock oscillations. However, other functions of FGF signaling have been described in the context of somitogenesis. In the previous section, I discussed how cellular motility or velocity could be related to oscillation dynamics.

In addition, FGF signaling has roles described as setting the wavefront or the determination front in the PSM. In the clock and wavefront model [Cooke and Zeeman (1976)], cells anterior to the wavefront are permitted to differentiate into a somite with each activity of the clock. A threshold in FGF signaling level is proposed to correspond to the wavefront, instructing the positions of segment boundaries [Dubrulle et al. (2001); Sawada et al. (2001)]. In this context, the regulation of Mesp2, a gene marking the initiation of segmentation is of particular interest. Mesp2 expression is dependent on NICD, Tbx6 (expressed in PSM) and the release from FGF and Wnt signaling [Aulehla et al. (2008); Niwa et al. (2011)]. The expression of Mesp2 could indeed be regulated by the level of FGF signaling present in the cell, performing a wavefront function. How does the additional role of FGF regulating oscillation dynamics fit into this scheme?

If oscillation dynamics and the positioning of segment boundaries are independent, there are no issues to resolve. However, there is evidence suggesting that oscillation dynamics are functionally relevant for segment patterning [Lauschke et al. (2013); Sonnen et al. (2018)]. In [Lauschke et al. (2013)] it was reported that in the mPSM, segment boundaries occur in the periphery at positions of 2π phase shift from the center in terms of LuVeLu oscillations. In [Sonnen et al. (2018)] it was further reported that the Axin2T2A-Luciferase reporter (Wnt signaling) and the LuVeLu reporter (Notch signaling) oscillate out of phase in the posterior (central) mPSM, but occurs in phase at the anterior (peripheral) regions. An out of phase relationship of *Axin2* and *Lfng* oscillations had also been reported in the intact mouse PSM in the tailbud region [Aulehla et al. (2003)]. Therefore it was proposed that oscillation phase shift between Wnt and Notch expression encodes for positional information, and segment boundaries are formed where Wnt and Notch oscillations occur in phase. In other words, this suggests that the phase shift between Wnt and Notch signaling encodes for the maturity or differentiation status of the PSM cell.

Using the dynamic alpha model I have proposed that FGF signaling could control how the two oscillators (Wnt and Notch) develop their phase difference. If phase difference encodes for maturity, then FGF signaling could be understood as an upstream signal controlling differentiation. Models describing FGF as the wavefront suggests that cells that fall below a certain threshold level of FGF signaling are allowed to differentiate into somites. A key difference between the two models is that in the former, FGF controls the *speed* of maturation, while in the latter FGF levels directly define maturation status. However, both hypotheses share general predictions, such as delayed differentiation upon increased FGF signaling. In any case, a critical experiment would be to test if cells can differentiate at varying levels of FGF signaling. The former suggests that absolute levels are not critical, while the latter proposes that cells would differentiate only when below a threshold level of FGF.

In reality, both hypotheses could be correct. Perhaps some pathways (expression of Mesp2) read out the level of FGF signaling, and others (oscillation phase shift) read out the temporal integral of FGF signaling. Both may need to coincide properly to coordinate the expression of segment boundary genes and the arrest of oscillations, such that the segmentation program can continue to the physical separation of somites. In [Sonnen et al. (2018)], Wnt and Notch

oscillations were each controlled by entrainment techniques to force the oscillations to occur in anti-phase at the anterior (peripheral) mPSM. In this case, oscillation arrest was postponed at the periphery, but Mesp2 expression proceeded normally, showing that these processes can be decoupled. As a result, morphological boundary formation is impaired, showing that oscillatory dynamics are also instructive for segmentation. FGF signaling may indeed be a hub that orchestrates specific gene expression and oscillation behavior for proper segmentation.

CHAPTER 7

Conclusion

How are wave dynamics regulated? This question prompted me to study somitogenesis, and I have held onto it since. The emergence of traveling waves from initial synchrony in the mPSM was astonishing. As I studied further, it seemed that PSM cells have an intrinsic capacity, or almost an obsession, to generate traveling waves. I focused on two contexts which both show emerging traveling waves; the gastrulating mouse embryo and the mPSM, to unveil the mechanism of this capacity.

Using the methodology that Henning Falk developed, I also imaged the onset of segmentation clock dynamics and observed its specific mode of generating the first traveling waves. It was a challenge to devise the correct method to extract oscillatory dynamics (i.e. surface kymographs) but this was necessary to argue for an oscillation period gradient at the tissue level. It turns out that measurement methods of oscillation dynamics are not consolidated, and pitfalls such as the introduction of artificial Doppler effects exist. Taking the golden standard to be single cell oscillation measurements tracked over space and time, I attempted to mimic this measurement to the best of my abilities, utilizing cell movement data from [McDole et al. (2018)]. I showed that period measurements obtained in this manner are graded already at the second cycle of oscillations, with a concave shape as predicted by theoretical studies.

Demonstrating that this rather intricate imaging technique can be passed on from its designer indicates its reproducibility and reliability. Critically, it opens up avenues to study previously inaccessible problems at the periphery of gastrulation. For any mutant phenotype of oscillation dynamics, we are now able to visualize the stage at which it manifests.

However, it is essential that optimization of the imaging protocol is pursued. Especially with the advent of brighter reporter lines, lowering phototoxic effects while keeping imaging quality should be a feasible goal. As this imaging technique has the potential to achieve comparable culture outcomes as the standard roller culture, this should be the ultimate goal of evolving this protocol.

I turned to study the in vitro mPSM to further dissect the question of how traveling waves emerge. In a phenomenological sense, this particular model mimics the gastrulating mouse embryo. ex vivo tail culture assays are well studied, but the preestablished wave patterns and signaling gradients constitute unnecessary parameters to be assumed. The mPSM represents a "reduced" system where at timepoint 0, its wave dynamics are reinitialized.

I characterized the effect of exogenous FGF signal on the dynamics of the segmentation clock in detail. The analysis was performed systematically by focusing on the parameter of phase

gradient slope, which accurately integrates and represents the spatiotemporal dynamics. Both temporally regulated (ad hoc addition) and spatially regulated (FGF bead) experiments were performed, yielding unexpected results. The data combined suggests that FGF signaling does not directly correlate with oscillation period as previously proposed, but changes a rather hidden parameter α, controlling the *speed* of change in oscillation dynamics (phase and period).

It is critical to test whether the findings made with the in vitro mouse model still hold outside of its context. Several parameters including α values at different FGF concentrations were estimated in this research, which can be used to generate models predicting the outcomes in ex vivo tail culture, as well as with the gastrulating stage. The model would be useful to design specific experiments to differentiate if FGF controls period or α. In addition, as FGF gradients and Notch pathway oscillations are conserved across species, and also as the model is purely phenomenological and without any molecular constraints, it can be tested in a wide variety of species and contexts.

I hope to have clarified an initial approach to uncover the relationship between the gradient and the clock in somitogenesis. These two entities, initially thought to be independent, turn out to be intricately connected. Coupling these factors implicate the coupling of cellular movement and oscillation dynamics, or at the macroscopic scale, axial growth, and waveform dynamics. Such a connection may be beneficial for evolution, for instance, to change growth rate while keeping patterning unperturbed.

To conclude I have provided a part of the answer to my initial question: how are wave dynamics regulated? The complete picture is still far but the outlines are becoming clear. Perhaps the last obstacle would be to integrate intercellular coupling, still enigmatic and notoriously fascinating. One day, I hope to see a full choreography of the dancing waves in the developing vertebrate embryo.

CHAPTER 8

Materials and methods

8.1 Mouse lines

Following mouse lines used in this study were described previously: LuVeLu [Aulehla et al. (2008)], Dusp4-T2A-3xmVenus [Falk (2018)], Lfng-T2a-3xmCherry[Falk (2018)]. The Dusp4-T2A-3xmVenus line was generated at EMBL Heidelberg by Nobuko Tsuchida-Straeten and Yvonne Peterson. All mouse lines were kept in an outbred background, and housed in the EMBL animal facilities.

All animal experiments were conducted after project approval by the Institutional Animal Care and Use Committee (IACUC) and under veterinarian supervision, following the guidelines of the European Commission, Directive 2010/63/EU and AVMA Guidelines 2007.

The following materials and methods pertain to "Part II The onset of segmentation clock oscillations in the gastrulating mouse embryo."

8.2 *In situ* hybridization chain reaction (HCR)

RNA *in situ* hybridization chain reaction (HCR) was performed as previously described [Choi et al. (2018)] with adaptations for mouse embryo tissue as detailed in [Sanchez et al. (2019); Sanchez (2020)]. In addition, the modification of treating samples with 10 µg/ml proteinase K (Merck, CAS #38450-01-6) for 3 minutes at room temperature (~25°C) was made to prepare E8.5 whole mouse embryos. Probe sequences used for *Msgn1*, *Uncx4.1*, *Shh* are provided in the following table. Nuclei were stained with 5 µg/ml DAPI diluted in 5x SSCT solution for 3x 30 min.

target gene	ID	sequence
Msgn1	Even 01	ctcactcccaatctctataaTCCTCCAGGCTGAGGAAGGTCTCAC
	Odd 01	CCAGCGGTGTCAGAAGAGTCCAGGCaactaccctacaaatccaat
	Even 02	ctcactcccaatctctataaGAAGGAGCTGGGGAGAGGCTTTGAG
	Odd 02	AGTGCGACCTCAGAGTAGGACTCCAaactaccctacaaatccaat
	Even 03	ctcactcccaatctctataaAGCCAACATGCTGTAATCCAGCTCG
	Odd 03	AGCAGTGTGTAGATAGGGAGGTTGAaactaccctacaaatccaat
	Even 04	ctcactcccaatctctataaAGTTTCTCTCTCTCGCTGGCCTTCC
	Odd 04	AGGGCATCGGCTAAGGTCCGCATCCaactaccctacaaatccaat
	Even 05	ctcactcccaatctctataaTGTACTTGAGTGTCTGGATCTTGGT
	Odd 05	CTGTGAGTTCCCCGATGTACTTGATaactaccctacaaatccaat
Shh	Even 01	cctcgtaaatcctcatcaaaACTTGTGAGCTGTCCCCGCGCTGTC
	Odd 01	GCAGCATCTCGTCCGCGGAACCTGAaaatcatccagtaaaccgcc
	Even 02	cctcgtaaatcctcatcaaaTACTTGCTGCGGTCCCGGTCGGACG
	Odd 02	TCCACAGCCAGGCGAGCCAGCATGCaaatcatccagtaaaccgcc
	Even 03	cctcgtaaatcctcatcaaaGAGAATGGTGCCGTGCGCCGTGAGC
	Odd 03	GTAGCACGAGGCGAGCACCCGGTTGaaatcatccagtaaaccgcc
	Even 04	cctcgtaaatcctcatcaaaCCTTATAGTCTACTTTGGACTGCCC
	Odd 04	CAACAGAACTCCCCGGGGTTTTTGCaaatcatccagtaaaccgcc
	Even 05	cctcgtaaatcctcatcaaaCAAACCAAGAAGGCAGTACAGAAGA
	Odd 05	GACAAAGTGGCGGTTACAAAGCAAAaaatcatccagtaaaccgcc
Uncx4.1	Odd 01	cctcaacctacctccaacaaTGAAGGGCTGGCTTTCGCCGGCCAC
	Even 01	TGTCTGGATCCCCCGAGTCTGCAAGattctcaccatattcgcttc
	Odd 02	cctcaacctacctccaacaaTGCCAGCCGGTAAAGTTGGTGCGGG
	Even 02	TTGAACGCCTTCTCCAGCTCCTCCAattctcaccatattcgcttc
	Odd 03	cctcaacctacctccaacaaGATTTTGGAACCAGACCTGAACTCG
	Even 03	TCTCCTTCTTTCTCCATTTGGCCCGattctcaccatattcgcttc
	Odd 04	cctcaacctacctccaacaaGAGCAGTTTCTTCTCGTGTTTGCGT
	Even 04	CGAGTGCAGGTGGCGGCTCTGACTCattctcaccatattcgcttc
	Odd 05	cctcaacctacctccaacaaTAGCCTTAGGCAGGCCCGCAGTCGC
	Even 05	ACAGCAGGCTCTCCACGCTGAACGGattctcaccatattcgcttc
	Odd 06	cctcaacctacctccaacaaCCAATCAGGGTCCGAGGTGCACACG
	Even 06	ATGGGGTAGAGCAAGAAGTGGCCCTattctcaccatattcgcttc
	Odd 07	cctcaacctacctccaacaaTGGCCCGGGAGAGGCAACAACCTCA
	Even 07	TAGGTCCCGGAAAGAAGCGGGAGCGattctcaccatattcgcttc
	Odd 08	cctcaacctacctccaacaaGTCCATGTCCACCTCCTCGCCCTCG
	Even 08	CATCTTCCAGCCGCGGTCCCCAGCTattctcaccatattcgcttc
	Odd 09	cctcaacctacctccaacaaACCTCACCCCAGGACCAGCAGCTGC
	Even 09	GGTTTTTTGATCCCTCCGGAGGAGGattctcaccatattcgcttc
	Odd 10	cctcaacctacctccaacaaTGTGGGTTTTGTGTGTGTGTGTGTG
	Even 10	GCATTTTACAAGGCTGAGGATTCTCattctcaccatattcgcttc

8.3 Mounting and Imaging of *In situ* hybridization chain reaction (HCR) samples

E8.5 whole mouse embryos stained with HCR were dissected to remove extraembryonic tissue. Samples were placed in a fructose-glycerol clearing solution described in [Dekkers et al. (2019)] over night at 4°C. Tissue rostral to the heart field was removed, and the remaining embryo

was mounted flat onto a glass slide with the dorsal side down in the fructose-glycerol clearing solution. A coverslip was placed on top of the sample using plaster for support, and enclosed with top coat. Imaging was taken on an LSM 780 laser-scanning microscope (Carl Zeiss Microscopy) with the following settings.

parameter	value
objective lens	Plan-Apochromat 20x/0.8
zoom	0.6x
image size	512 x 512 pixel x 2 x 3 tile
xy resolution	1.384 µm/pixel
z interval	8 µm
z stack	17 slices
pixel dwell	12.61 µsec

parameter	DAPI imaging	Alexa488 imaging
excitation	405nm (30mW Diode laser)	488nm (25mW Argon laser)
laser power	0.4%	8.0%
emission detection	410-585nm	500-560nm
pinhole	1.9 µm section	2.0 µm section

parameter	Alexa546 imaging	Alexa647 imaging
excitation	561nm (20mW DPSS laser)	633nm (5mW Helium-neon laser)
laser power	1.2%	5.0%
emission detection	560-638nm	638-7555nm
pinhole	1.6 µm section	4.6 µm section

8.4 Embryo dissection and mounting

E7.5 mouse embryos were dissected and mounted onto glass capillaries as previously described in [Falk (2018)]. Embryos were mounted with either the posterior side or distal end facing the objective to visualize LuVeLu signal in the mesoderm, for phototoxicity assessment (section 3.1) and oscillation dynamics analysis (section 3.2), respectively.

8.5 Embryo culture and imaging on the light-sheet microscope

E7.5 mouse embryos were imaged on the Lightsheet Z.1 (Carl Zeiss) as previously described in [Falk (2018)], with the following settings:

parameter	value
objective lens	20x 1.0NA Plan-Apochromat water immersion objective (Carl Zeiss)
zoom	0.41x
image size	1920 x 1920 pixel at 16-bit
xy resolution	0.545 µm/pixel
z interval	7.5 µm
z stack	100 (posterior mounting) or 150 (distal mounting) slices
excitation	514nm (50 ~mW internal laser power)
laser power	2.0%
exposure time	299.6 msec
emission selection	short band side of long pass filter at 560nm, bandpass at 505-545nm
imaging interval	10 min
imaging duration	~24 hours

8.6 Time series registration

8.6.1 Downsizing

The online dual side fusion function on the ZEN software (Carl Zeiss Microscopy GmbH) was used to fuse images taken sequentially with the two sides of light sheet illumination. The images were then downsized in the xy dimension by a factor of three using the average function in ZEN. Images were further downsized in the xy dimension by a factor of 1.25 using a script run on ImageJ/Fiji [Schindelin et al. (2012)].

8.6.2 Temporal background reduction

The following text was written by Takehito Tomita in [Falk et al. (2021)] in revision:

"A fixed 30 x 30 x 150 voxel (xyz) in the data outside the embryo was averaged to obtain the background value for each time frame, then subtracted from the entire image. An offset value of 1000 intensity counts was added subsequently to the image uniformly."

8.6.3 Time series registration

Image registration was done as previously described in [Falk (2018)], using a script developed by Christian Tischer (available on https://github.com/tischi/fiji-script-registrationUsingElastix).

8.7 Surface kymographs

For kymographs analyzed in sections 3.2 and 3.3, the curved surface of the mesoderm was followed along the propagation direction of waves with the following strategy.

The following text was written by Takehito Tomita in [Falk et al. (2021)] in revision:

"After registration, the datasets were resized in the Z dimension by a factor of 3.59 to obtain isotropic resolution in X,Y, and Z. The datasets were then thresholded with a value of 1030 to make binary masks for each timepoint. These masks were summed for all timepoints, and its center of mass (COM) was calculated to be used as the center coordinate of the embryo. The entire 3D+t dataset was translated so that the COM coordinate matched the

center of the image, then rotated with manually defined angles around the COM such that the anterioposterior and proximodistal axes matched the Y and Z axes, respectively.

3D coordinates of the proximal oscillation origin and distal ends of the PSM on both sides were manually marked throughout the time series in several key frames, then linearly interpolated for the intermediate timepoints. For each timepoint, the midpoint between the origin and a distal end were calculated. From the image, line profiles extending the vector from the COM to the midpoints were obtained, and the coordinate with the maximum intensity in this line profile was recorded for all timepoints. A spline was fit to these coordinates through time, and its values were used to designate the coordinate of an intermediate point on the mesoderm surface between the oscillation origin and the distal end of the PSM for each timepoint.

A spline was fit through these three points (proximal oscillation origin, intermediate point, and distal end) at each timepoint to be used as the line of interest. To calculate the distance of the arc between the proximal oscillation origin and the distal end, we took a chorded approximation approach by dividing the arc into 100000 piecewise linear segments with equal division of the spline parameter u = [0,1]. The cumulative sum of these segment lengths were stored in a table with the corresponding parameter value, and the total sum was stored as an estimate of the total arc length. The u value giving the closest cumulative distance to each integer distance was determined from the table for all integers below the total arc length. Points on the arc with these u values were used to collect values for the kymograph, so that one spatial pixel on the kymograph corresponds to one pixel distance on the arc. To collect intensity values, the 3D dataset was smoothed with a 3D Gaussian (σ=6pixels ≈12.5 µm) and intensity was averaged within a spherical volume centered at each point with a diameter of 12 pixels ≈25 µm. The kymograph was constructed by fixing the intensity time series from the origin at the midline and extending the values collected from the left and right arcs on top and bottom of the midline, respectively.

All computational steps described here for surface kymograph generation were implemented in the Python programming language, making extensive use of the 'SciPy' library [Jones et al. (2001)] and 'OpenCV' library [Bradski (2000)]."

8.8 Phase Kymographs

The following text was written by Takehito Tomita in [Falk et al. (2021)] in revision:

"For each surface kymograph, the timepoint at which the waves began after the LuVeLu 'pulse' was determined manually. The preceding frames were cropped out for the subsequent phase extraction. Regions outside the kymograph (regions exceeding the total spline length at each timepoint) were filled with a background value of 1067. The intensity kymographs were smoothed with a Gaussian in the spatial dimension (σ= 5pixels ≈10.4 µm)."

The following text was written by Henning Falk, Gregor Mönke, and Alexander Aulehla and taken from [Falk et al. (2021)] in revision:

"Phase extraction from the raw intensity kymographs was done using Wavelet transforms [Torrence and Compo (1998)]. To remove low-frequency trends, every row (in the following called time-series) of a kymograph was convolved with a Sinc filter with a 'cut-off-period' of 220 min. Sinc filters are designed to be optimal low-pass filters in the frequency domain (Smith, 1997). The results from the convolution were then subtracted from the original time series. These detrended time series were then convolved with 600 complex Morlet Wavelets,

scanning periods from 100 to 220 min. By tracing the power-maxima in the Wavelet spectra over time, the so called 'ridges' were identified. Evaluating the complex Wavelet transforms along the ridges gave a complex signal for every time series. Finally, by extracting the argument from these complex signals, the phase values over time were obtained. Re-stacking these phase-valued time series produced the phase kymographs.

The module of wavelet transform for time series used in this study is available as pyBOAT [Mönke et al. (2020)] (available on https://github.com/tensionhead/pyBOAT)."

8.9 Phase gradient slope and wave number q

The following text was written by Takehito Tomita in [Falk et al. (2021)] in revision:

"For all measurements made for wave number, only the left side of the embryo, or the top half of the kymograph was used.

The phases along a column of the phase kymographs were first unwrapped to obtain continuous phase values. At each column, 20 pixels at the distal end were cropped off. The phase difference between the distal end and midline were taken and divided by 2π to obtain wave numbers (Fig. 3.2E). The length of the cropped column, corresponding to spline length on the surface of the mesoderm, was used as mesoderm length (Fig. 3.2D). The wave number was divided by the mesoderm length at each timepoint to obtain the linear estimate of the phase gradient slope (Fig. 3.2F). "

8.10 Cell movement extraction from *in toto* cell tracking datasets

The following text was written by Takehito Tomita in [Falk et al. (2021)] in revision:

"To extract cell movement from the *in toto* cell tracking datasets presented in [McDole et al. (2018)], we first temporally aligned each of the four datasets in relation to the LuVeLu imaged embryos by designating a timepoint corresponding to the peak of the "pulse" stage. This timepoint was manually determined by comparing the extent of mesoderm ingression and the diameter of the embryo between the two datasets. t=0 corresponding to the start of waves were designated to be 260 min after the peak of the "pulse" for each embryo. Next, using the landmark annotations made on the cell tracking datasets, a plane bisecting the embryo at the midline was defined for every timepoint. The proximal oscillation origin location was estimated by an algorithm using the designated cell fates as input. We summarized the line of interests used on the LuVeLu embryos to obtain the kymographs by averaging the distal control points for each timeframe, using the proximal control points as a common reference. The trajectory of the average distal points was smoothed through time using a spline. The average distal points were projected on the cell tracking datasets from the estimated oscillation origin locations, then adjusted so that these points were located within the mesoderm region. Using the origin points and distal points, intermediate points were defined, then the line of interests were reproduced on each of the cell tracking datasets following a similar algorithm as described in *Surface Kymographs*.

The line of interest was used to collect annotated mesoderm cells in each dataset which stayed within 30 µm to the line for over 300 consecutive minutes. At each timepoint, the nearest point on the line of interest was found for each cell, and its distance from the origin point was

calculated using the chorded approximation approach described above in *Surface Kymographs*. Using the origin point and t=0 as a common reference, the acquired trajectories were averaged into vector flows for partitioned time and space blocks, either with all four datasets (Fig. 3.3C) or individually (Fig. 3.3B). The final streamline plot was generated from the vector field using the built-in function in the 'Matplotlib' library.

All computational steps described here for extracting the cell movement data were implemented in the Python programming language. Visualizations (Fig. 3.3A) were done using Blender (available on http://www.blender.org)."

8.11 Periods

The following text was written by Takehito Tomita in [Falk et al. (2021)] in revision:

"For measurements made for period, only the left side of the embryo, or the top half of the kymograph was used.

To calculate periods from proximal to distal, Cell velocities were first estimated from the cellular flows obtained from analyzing data from [McDole et al. (2018)]. The most distal cells (200 µm from the proximal area at t=0) were estimated to move with a velocity of 0.34 µm/min from the proximal area. The proximal area was set to have a velocity of 0 µm/min, and the velocity at the areas in between was linearly interpolated.

The estimated cell flow trajectories were then overlaid to the LuVeLu kymographs, with ten starting positions interpolated between 0 µm and 110 µm from the proximal area (Fig. 3.3E). Velocity from the previous estimation was used according to the starting position. The intensity values of LuVeLu signal were taken as input time series for each trajectory. These time series were subsequently analyzed by Wavelets as described above (*Phase Kymographs*). The periods were extracted along the maxima ridges of the Wavelet spectra.

Period values during 2~6 hours after the initiation of waves were collected as data points (24 points per embryo per region), which were used to calculate median and IQR for (Fig. 3.3F)."

8.12 Selection criteria for sample sizes

The following text was written by Takehito Tomita in [Falk et al. (2021)] in revision:

"For the assessment of culture outcome (section 3.1), no selection of embryos were made. 6/6 SPIM imaged embryos, 5/6 non-imaged SPIM cultured embryos and 17/17 roller culture embryos over three independent imaging experiments were considered for (Fig. 3.1A,B). One embryo for the non-imaged SPIM cultured group was lost during the RNA *in situ* hybridization chain reaction (HCR) process, hence the 5/6 usage of samples in this group.

For the quantitative analyses made for (section 3.2, 3.3), a total of eight embryos carrying the LuVeLu reporter were imaged in two independent experiments. Of these eight embryos, five embryos were used for the final analysis. Of the three embryos omitted from the analysis, one embryo showed weak LuVeLu expression and no visible oscillations. The remaining two omitted embryos showed visible LuVeLu oscillations, however either moved out of the field of view during imaging, or was not imaged long enough to capture 800+ min of oscillation dynamics and was therefore omitted from analysis.

No selection of embryos based on sex were made throughout this study."

The following materials and methods pertain to "Part III The effect of FGF signaling on segmentation clock dynamics."

8.13 Dissection and culture medium

0.5 mM glucose, 2 mM glutamine and 1% BSA was added to DMEM-F12 (Cell Culture Technologies). 10 mM HEPES was added to this solution to be used as dissection medium. For culture medium, no HEPES was added and the solution was filter sterilized through a 0.22 µm filter (Millex-GV, Cat.No: SLGV033RS) and 100U/ml Penicillin/Streptomycin (Gibco, Cat.No: 15140-122) was added. Culture medium was equilibrated in 37 °C 5% CO_2 until use.

8.14 Preparation of FGF8b ligand

Recombinant Human/Mouse FGF8b Isoform ligand was purchased from R&D systems (Cat.no.: 423-F8-025). 25 µg FGF8b ligand was dissolved in 25 µl 0.1%BSA/PBS at a concentration of 1 µg/ µl. The solution was aliquoted into 2-4 µl portions and stored at -20°C until use.

8.15 Washing of heparin-agarose beads

Heparin-agarose beads were purchased from Sigma (Cat.No: H0402-5ML). 150 µl bead solution was added to 750 µl PBS, and mixed well on a roller at 4°C for 30 min. The solution was centrifuged at 20817 rcf for 1 min. 750 µl supernatant was removed, and new 750 µl PBS was added. This washing process was repeated three times in total. After the last washing step, ~800 µl of supernatant was removed. The washed bead solution was stored in 4 °C until use.

8.16 Preparation of fluorescent beads

To fluorescently label heparin-agarose beads, Mix-n-Stain™ CF® Dye Antibody Labeling Kits were purchased from Biotium (Cat.No: 92277). 90 µl of washed bead solution was mixed with 10X Mix-n-Stain™ Reaction Buffer, then mixed with the CF®633 dye solution. The mixture was incubated for 30 min in the dark at room temperature (~25°C). The labeled bead solution was moved to Storage Buffer and stored in 4 °C in dark until use.

8.17 Preparation of FGF beads

To coat fluorescently labeled Heparin-agarose beads with FGF8b ligand, 1 µl of the fluorescent bead solution was mixed with 4 µl 1 µg/µl FGF8b ligand solution, and incubated overnight (~12 hours) in the dark at room temperature (~25°C). To prepare control beads, 4 µl 0.1%BSA/PBS solution was used instead of the FGF8b ligand solution. Beads were washed twice in equilibrated culture medium shortly before use, to remove residual FGF8b ligand.

8.18 Fibronectin coating

8.18.1 For FGF medium addition experiments

The wells of 8-well plate (Nunc™ Lab-Tek™ II Chambered Coverglass, Cat.No: 155409PK) were filled with ~160 µl of 50 µg/ ml fibronectin (Sigma, Cat.No: F1141) diluted in PBS, and incubated for 1 hour in 37 °C. The fibronectin solution was removed, and the plate was dried for 1 hour at room temperature (~25°C). The wells were washed once with culture medium, then filled again with culture medium for the experiment.

8.18.2 For FGF bead experiments

Ibidi micro-Inserts 4 Well FulTrac for self insertion (Ibidi, Cat.No: 80489) were placed in 2-well plate (Nunc™ Lab-Tek™ II Chambered Coverglass, Cat.No: 155379PK), and placed in vacuum (70kPa) for 10 min. The wells were each filled with ~20 µl of 50 µg/ ml fibronectin (Sigma, Cat.No: F1141) diluted in PBS and incubated for 1 hour in 37 °C. The fibronectin solution was removed, and the plate was placed in vacuum (70kPa) again for 10 min. The wells were washed once with culture medium, then filled again with culture medium for the experiment.

8.19 2-D ex vivo segmentation assay using the mPSM

2-D ex vivo segmentation assays using the mPSM were performed as previously described in [Lauschke et al. (2013)].

8.20 FGF addition experiment procedures

8.20.1 Continuous FGF addition experiments

1 µg/µl FGF8b ligand solution was diluted with culture medium to obtain 16/15x2 µg/ml, 16/15x4 µg/ml or 16/15x 8 µg/ml FGF8b ligand solution. 300 µl of this conditioned medium was added to each well in the 8-well plate, and the mPSMs were moved into the well with 20 µl culture medium to finally obtain a concentration of 2 µg/ml, 4 µg/ml or 8 µg/ml FGF8b. The mPSMs were allowed to attach for at least 1 hour in 37 °C 5% CO_2 before imaging was initiated.

8.20.2 FGF medium reuse experiments

mPSM samples were cultured with 8 µg/ml FGF8b as described above. After 48 hours of culture, the remaining medium (~300 µl) was collected. Fibronectin coated plates were freshly prepared, and filled with collected medium. Fresh mPSMs were moved into this well with 5 µl culture medium and were allowed to attach for at least 1 hour in 37 °C 5% CO_2 before imaging was initiated.

8.20.3 ad hoc FGF addition experiments

mPSM samples were cultured and imaged with 0, 4, or 8 µg/ml FGF8b as described above. After 16 or 24 hours of culture, the medium was completely removed from the well, and quickly replenished with 300 µl freshly prepared medium of 0, 4, or 8 µg/ml FGF8b. The imaging was paused during the medium switch, and one frame in the 10 min interval was not acquired. This frame was reconstituted digitally by linearly interpolating between the preceding and succeeding frames.

8.20.4 FGF bead experiments

Either FGF beads or control beads were moved into the wells of 4 Well FulTrac insertions. The mPSM was carefully laid on top of the bead and allowed to attach for at least 1 hour in 37 °C 5% CO_2 before imaging was initiated. ~2ml culture medium was added to completely submerge the FulTrac insertion.

8.21 PD0325901 addition experiments

PD0325901 was purchased from Sigma (Cat.No: PZ0162) and dissolved in DMSO to a concentration of 50mM. This solution was diluted with culture medium to a concentration of 6, or 18 µM. 300 µl of this conditioned medium was added to each well in the 8-well plate, and the mPSMs were moved into the well with 10 µl culture medium. The mPSMs were allowed to attach for at least 1 hour in 37 °C 5% CO_2 before imaging was initiated.

8.22 Confocal microscopy of mPSM

Prepared mPSM samples were imaged on the Zeiss LSM780 laser-scanning microscope with the following settings, with environmental control keeping 37 °C 5% CO_2 condition in the imaging chamber:

parameter	value
objective lens	Plan-Apochromat 20x/0.8
zoom	0.6x
image size	512 x 512 pixel
xy resolution	1.384 µm/pixel
imaging interval	5 or 10 min
imaging duration	~56 hours

parameter	Venus imaging	CF633 imaging
z interval	8 µm	6 µm
z stack	4-11 slices	15 slices
excitation	514nm (25mW Argon laser)	633nm (5mW Helium-neon laser)
laser power	2.0%	6.0%
pixel dwell	3.15 µsec	1.58 µsec
emission detection	517-577nm	638-758nm
pinhole	5.6-9.5 µm section	1.3 µm section

parameter	mCherry imaging
z interval	8 µm
z stack	4 slices
excitation	561nm (20mW DPSS laser)
laser power	4.0%
pixel dwell	3.15 µsec
emission detection	576-690nm
pinhole	9.5 µm section

8.23 Kymograph generation

8.23.1 For FGF medium addition experiments

The following processes were done in ImageJ/Fiji [Schindelin et al. (2012)]. To generate kymographs, images were first projected in the z dimension for maximum intensity and smoothed with a Gaussian (σ=5pixels ≈6.9 μm) at each time frame. Using the KymoResliceWide plugin developed by Eugene Katrukha (available at https://github.com/ekatrukha/KymoResliceWide), kymographs were generated with a width of 20 pixels ≈ 27.7 μm, from the wave center to the periphery.

8.23.2 For FGF bead experiments

The following processes were done in the Python programming language. To generate kymographs, images were first projected in the z dimension for maximum intensity and smoothed with a Gaussian (σ=5pixels ≈6.9 μm) at each time frame using the scipy.ndimage.filters package. The coordinates for wave center, bead position, and the mirrored position of the bead (as control side) were determined manually. Using the profile_line function from the skimage.measure package, kymographs were generated with a width of 20 pixels ≈ 27.7 μm, from the wave center to either towards the bead position or mirrored position. The line of interest was extended up to a length of 400 pixels, such that it included positions peripheral to the bead position and mirrored position.

8.24 Phase and period kymograph

Phase and period kymographs were generated similarly as previously described in "Phase kymographs." The intensity kymographs were first smoothed with a Gaussian in the spatial dimension (σ= 10pixels≈13.8 μm). A Sinc filter with a cutoff period of 220 min was used to detrend the time intensity profiles, then convolved with 600 complex Morlet Wavelets scanning periods from 100 min to 220 min. The phase and period values obtained were re-stacked to produce phase and period kymographs, respectively.

8.25 Masking of kymographs

Masking of LuVeLu and Dusp4-T2A-3xmVenus kymographs were done manually in ImageJ/Fiji [Schindelin et al. (2012)], by selecting the oscillatory region. Embryos used for the Dusp4-T2A-3xmVenus reporter also expressed the Lfng-T2a-3xmCherry reporter, indicating oscillatory area. The signal from this reporter was used to mask oscillatory area for these samples when available, for Fig. 5.4B. Morphological features in the bright field channel were used to estimate the mask when Lfng-T2a-3xmCherry reporter quantification was unavailable, for Fig. 5.4C.

8.26 Extraction of phase gradient data

8.26.1 For FGF medium addition experiments

At each timepoint, the corresponding column of the phase kymograph was extracted as the phase gradient. The vector was masked to remove non oscillatory regions and unwrapped

to remove jumps in phase. The phase span was calculated as the difference between the maximum and minimum phase values within this unwrapped vector, and divided by 2π to obtain the wave number. A linear fit was made to the unwrapped phase vector to obtain the slope using the linear_model function from the sklearn package. The length of the mask was used as the length of the oscillatory area.

8.26.2 For FGF bead experiments

The phase gradient was extracted similarly as above, and aligned spatially to the bead position. The position 30pixels ≈41.5 μm inward to the wave center from the bead position was used as the reference position, and all phase gradients were normalized such that this position had a phase value of zero. The mean and standard deviation were calculated at each position, where four or more samples had values for the phase gradient. For the control side, the position with the same distance from the wave center to the bead on the contralateral side was used instead as the bead position.

8.27 Extraction of period data

Period values at the central and peripheral areas were extracted from the period kymographs. The peripheral area was defined as 5 pixels ≈6.92 μm inward from the peripheral edge of the mask, and the central area was defined as 4 pixels ≈5.53 μm inward from the central edge of the mask. The mean and standard deviation were calculated at each timepoint, where six or more samples had values for the period.

8.28 Extraction of Dusp4-T2A-3xmVenus gradient data

At each timepoint, the corresponding column of the Dusp4-T2A-3xmVenus kymograph was extracted as the Dusp4 activity gradient. The vector was masked to remove non oscillatory regions. The data from 5-10 hours in culture was obtained (30 timepoints per sample), and the mean and standard deviation was calculated at each position.

Bibliography

Aulehla, A. and Johnson, R. L. (1999). Dynamic Expression oflunatic fringeSuggests a Link betweennotchSignaling and an Autonomous Cellular Oscillator Driving Somite Segmentation. *Developmental Biology*, 207(1):49–61.

Aulehla, A. and Pourquié, O. (2010). Signaling Gradients during Paraxial Mesoderm Development. *Cold Spring Harbor Perspectives in Biology*, 2(2):a000869.

Aulehla, A., Wehrle, C., Brand-Saberi, B., Kemler, R., Gossler, A., Kanzler, B., and Herrmann, B. G. (2003). Wnt3a Plays a Major Role in the Segmentation Clock Controlling Somitogenesis. *Developmental Cell*, 4(3):395–406.

Aulehla, A., Wiegraebe, W., Baubet, V., Wahl, M. B., Deng, C., Taketo, M., Lewandoski, M., and Pourquié, O. (2008). A β-catenin gradient links the clock and wavefront systems in mouse embryo segmentation. *Nature Cell Biology*, 10(2):186–193.

Bénazéraf, B., Beaupeux, M., Tchernookov, M., Wallingford, A., Salisbury, T., Shirtz, A., Shirtz, A., Huss, D., Pourquié, O., François, P., and Lansford, R. (2017). Multi-scale quantification of tissue behavior during amniote embryo axis elongation. *Development*, 144(23):4462–4472.

Bénazéraf, B., Francois, P., Baker, R. E., Denans, N., Little, C. D., and Pourquié, O. (2010). A random cell motility gradient downstream of FGF controls elongation of an amniote embryo. *Nature*, 466(7303):248–252.

Bessho, Y., Hirata, H., Masamizu, Y., and Kageyama, R. (2003). Periodic repression by the bHLH factor Hes7 is an essential mechanism for the somite segmentation clock. *Genes & Development*, 17(12):1451–1456.

Bessho, Y., Sakata, R., Komatsu, S., Shiota, K., Yamada, S., and Kageyama, R. (2001). Dynamic expression and essential functions of Hes7 in somite segmentation. *Genes & Development*, 15(20):2642–2647.

Bradski, G. (2000). The OpenCV Library. *Dr. Dobb's Journal of Software Tools*.

Choi, H. M. T., Schwarzkopf, M., Fornace, M. E., Acharya, A., Artavanis, G., Stegmaier, J., Cunha, A., and Pierce, N. A. (2018). Third-generation in situ hybridization chain reaction: multiplexed, quantitative, sensitive, versatile, robust. *Development*, 145(12).

Cooke, J. and Zeeman, E. C. (1976). A clock and wavefront model for control of the number of repeated structures during animal morphogenesis. *Journal of Theoretical Biology*, 58(2):455–476.

Crossley, P. and Martin, G. (1995). The mouse Fgf8 gene encodes a family of polypeptides and is expressed in regions that direct outgrowth and patterning in the developing embryo. *Development*, 121(2):439–451.

Dale, J. K., Malapert, P., Chal, J., Vilhais-Neto, G., Maroto, M., Johnson, T., Jayasinghe, S., Trainor, P., Herrmann, B., and Pourquié, O. (2006). Oscillations of the Snail Genes in the Presomitic Mesoderm Coordinate Segmental Patterning and Morphogenesis in Vertebrate Somitogenesis. *Developmental Cell*, 10(3):355–366.

Dekkers, J. F., Alieva, M., Wellens, L. M., Ariese, H. C. R., Jamieson, P. R., Vonk, A. M., Amatngalim, G. D., Hu, H., Oost, K. C., Snippert, H. J. G., Beekman, J. M., Wehrens, E. J., Visvader, J. E., Clevers, H., and Rios, A. C. (2019). High-resolution 3D imaging of fixed and cleared organoids. *Nature Protocols*, 14(6):1756–1771.

del Corral, R. D., Olivera-Martinez, I., Goriely, A., Gale, E., Maden, M., and Storey, K. (2003). Opposing FGF and Retinoid Pathways Control Ventral Neural Pattern, Neuronal Differentiation, and Segmentation during Body Axis Extension. *Neuron*, 40(1):65–79.

Delaune, E. A., François, P., Shih, N. P., and Amacher, S. L. (2012). Single-Cell-Resolution Imaging of the Impact of Notch Signaling and Mitosis on Segmentation Clock Dynamics. *Developmental Cell*, 23(5):995–1005.

Delfini, M.-C., Dubrulle, J., Malapert, P., Chal, J., and Pourquié, O. (2005). Control of the segmentation process by graded MAPK/ERK activation in the chick embryo. *Proceedings of the National Academy of Sciences*, 102(32):11343–11348.

Deng, C. X., Wynshaw-Boris, A., Shen, M. M., Daugherty, C., Ornitz, D. M., and Leder, P. (1994). Murine FGFR-1 is required for early postimplantation growth and axial organization. *Genes & Development*, 8(24):3045–3057.

Dequéant, M.-L., Glynn, E., Gaudenz, K., Wahl, M., Chen, J., Mushegian, A., and Pourquié, O. (2006). A Complex Oscillating Network of Signaling Genes Underlies the Mouse Segmentation Clock. *Science*, 314(5805):1595–1598.

Dias, A. S., de Almeida, I., Belmonte, J. M., Glazier, J. A., and Stern, C. D. (2014). Somites Without a Clock. *Science*, 343(6172):791–795.

Diaz-Cuadros, M., Wagner, D. E., Budjan, C., Hubaud, A., Tarazona, O. A., Donelly, S., Michaut, A., Al Tanoury, Z., Yoshioka-Kobayashi, K., Niino, Y., Kageyama, R., Miyawaki, A., Touboul, J., and Pourquié, O. (2020). In vitro characterization of the human segmentation clock. *Nature*, 580(7801):113–118.

Downs, K. and Davies, T. (1993). Staging of gastrulating mouse embryos by morphological landmarks in the dissecting microscope. *Development*, 118(4):1255–1266.

Dubrulle, J., McGrew, M. J., and Pourquié, O. (2001). FGF Signaling Controls Somite Boundary Position and Regulates Segmentation Clock Control of Spatiotemporal Hox Gene Activation. *Cell*, 106(2):219–232.

Dubrulle, J. and Pourquié, O. (2004). fgf8 mRNA decay establishes a gradient that couples axial elongation to patterning in the vertebrate embryo. *Nature*, 427(6973):419–422.

Eckalbar, W. L., Fisher, R. E., Rawls, A., and Kusumi, K. (2012). Scoliosis and segmentation defects of the vertebrae. *WIREs Developmental Biology*, 1(3):401–423.

Falk, H. J. (2018). *Imaging the onset of the segmentation clock during mouse gastrulation*. PhD thesis, Ruperto-Carola University of Heidelberg, Heidelberg.

Falk, H. J., Tomita, T., Mönke, G., McDole, K., and Aulehla, A. (2021). Imaging the onset of oscillatory signaling dynamics during mouse embryo gastrulation. (manuscript in revision).

Forsberg, H., Crozet, F., and Brown, N. A. (1998). Waves of mouse Lunatic fringe expression, in four-hour cycles at two-hour intervals, precede somite boundary formation. *Current Biology*, 8(18):1027–1030.

Giudicelli, F., Özbudak, E. M., Wright, G. J., and Lewis, J. (2007). Setting the Tempo in Development: An Investigation of the Zebrafish Somite Clock Mechanism. *PLOS Biology*, 5(6):e150.

Gomez, C., Özbudak, E. M., Wunderlich, J., Baumann, D., Lewis, J., and Pourquié, O. (2008). Control of segment number in vertebrate embryos. *Nature*, 454(7202):335–339.

Goodwin, B. C. and Cohen, M. H. (1969). A phase-shift model for the spatial and temporal organization of developing systems. *Journal of Theoretical Biology*, 25(1):49–107.

Holley, S. A., Geisler, R., and Nüsslein-Volhard, C. (2000). Control of her1 expression during zebrafish somitogenesis by a Delta-dependent oscillator and an independent wave-front activity. *Genes & Development*, 14(13):1678–1690.

Ichikawa, T., Nakazato, K., Keller, P. J., Kajiura-Kobayashi, H., Stelzer, E. H. K., Mochizuki, A., and Nonaka, S. (2013). Live Imaging of Whole Mouse Embryos during Gastrulation: Migration Analyses of Epiblast and Mesodermal Cells. *PLOS ONE*, 8(7):e64506.

Ishimatsu, K., Takamatsu, A., and Takeda, H. (2010). Emergence of traveling waves in the zebrafish segmentation clock. *Development*, 137(10):1595–1599.

Jones, E., Oliphant, T., Peterson, P., and others (2001). SciPy: Open source scientific tools for Python.

Jouve, C., Iimura, T., and Pourquie, O. (2002). Onset of the segmentation clock in the chick embryo: evidence for oscillations in the somite precursors in the primitive streak. *Development*, 129(5):1107–1117.

Kageyama, R., Masamizu, Y., and Niwa, Y. (2007). Oscillator mechanism of notch pathway in the segmentation clock. *Developmental Dynamics*, 236(6):1403–1409.

Keller, P. J., Schmidt, A. D., Wittbrodt, J., and Stelzer, E. H. (2008). Reconstruction of Zebrafish Early Embryonic Development by Scanned Light Sheet Microscopy. *Science*, 322(5904):1065–1069.

Lauschke, V. M., Tsiairis, C. D., François, P., and Aulehla, A. (2013). Scaling of embryonic patterning based on phase-gradient encoding. *Nature*, 493(7430):101–105.

Lewis, J. (2003). Autoinhibition with Transcriptional Delay: A Simple Mechanism for the Zebrafish Somitogenesis Oscillator. *Current Biology*, 13(16):1398–1408.

Liu, P., Wakamiya, M., Shea, M. J., Albrecht, U., Behringer, R. R., and Bradley, A. (1999). Requirement for Wnt3 in vertebrate axis formation. *Nature Genetics*, 22(4):361–365.

Masamizu, Y., Ohtsuka, T., Takashima, Y., Nagahara, H., Takenaka, Y., Yoshikawa, K., Okamura, H., and Kageyama, R. (2006). Real-time imaging of the somite segmentation clock: Revelation of unstable oscillators in the individual presomitic mesoderm cells. *Proceedings of the National Academy of Sciences*, 103(5):1313–1318.

Matsuda, M., Yamanaka, Y., Uemura, M., Osawa, M., Saito, M. K., Nagahashi, A., Nishio, M., Guo, L., Ikegawa, S., Sakurai, S., Kihara, S., Maurissen, T. L., Nakamura, M., Matsumoto, T., Yoshitomi, H., Ikeya, M., Kawakami, N., Yamamoto, T., Woltjen, K., Ebisuya, M., Toguchida, J., and Alev, C. (2020). Recapitulating the human segmentation clock with pluripotent stem cells. *Nature*, 580(7801):124–129.

McDole, K., Guignard, L., Amat, F., Berger, A., Malandain, G., Royer, L. A., Turaga, S. C., Branson, K., and Keller, P. J. (2018). In Toto Imaging and Reconstruction of Post-Implantation Mouse Development at the Single-Cell Level. *Cell*, 175(3):859–876.e33.

McGrew, M. J., Dale, J. K., Fraboulet, S., and Pourquié, O. (1998). The lunatic Fringe gene is a target of the molecular clock linked to somite segmentation in avian embryos. *Current Biology*, 8(17):979–982.

Mönke, G., Sorgenfrei, F. A., Schmal, C., and Granada, A. E. (2020). Optimal time frequency analysis for biological data - pyBOAT. Technical report.

Morelli, L. G., Ares, S., Herrgen, L., Schröter, C., Jülicher, F., and Oates, A. C. (2009). Delayed coupling theory of vertebrate segmentation. *HFSP Journal*, 3(1):55–66.

Naiche, L. A., Holder, N., and Lewandoski, M. (2011). FGF4 and FGF8 comprise the wavefront activity that controls somitogenesis. *Proceedings of the National Academy of Sciences*, 108(10):4018–4023.

Niwa, Y., Shimojo, H., Isomura, A., González, A., Miyachi, H., and Kageyama, R. (2011). Different types of oscillations in Notch and Fgf signaling regulate the spatiotemporal periodicity of somitogenesis. *Genes & Development*, 25(11):1115–1120.

Oates, A. C. and Ho, R. K. (2002). Hairy/E(spl)-related (Her) genes are central components of the segmentation oscillator and display redundancy with the Delta/Notch signaling pathway in the formation of anterior segmental boundaries in the zebrafish. *Development*, 129(12):2929–2946.

Palmeirim, I., Henrique, D., Ish-Horowicz, D., and Pourquié, O. (1997). Avian hairy Gene Expression Identifies a Molecular Clock Linked to Vertebrate Segmentation and Somitogenesis. *Cell*, 91(5):639–648.

Riedel-Kruse, I. H., Müller, C., and Oates, A. C. (2007). Synchrony Dynamics During Initiation, Failure, and Rescue of the Segmentation Clock. *Science*, 317(5846):1911–1915.

Rohde, L. A., Bercowsky-Rama, A., Negrete, J., Valentin, G., Naganathan, S. R., Desai, R. A., Strnad, P., Soroldoni, D., Jülicher, F., and Oates, A. C. (2021). Cell-autonomous generation of the wave pattern within the vertebrate segmentation clock. Technical report.

Sanchez, P. G. L. (2020). *Entrainment of coupled, phase-shifted signaling oscillations in the presomitic mesoderm*. PhD thesis, Ruperto-Carola University of Heidelberg.

Sanchez, P. G. L., Miyazawa, H., and Instruments, M. (2019). Hybridization chain reaction (HCR) protocol for tails of mouse embryos.

Sawada, A., Shinya, M., Jiang, Y.-J., Kawakami, A., Kuroiwa, A., and Takeda, H. (2001). Fgf/MAPK signalling is a crucial positional cue in somite boundary formation. *Development*, 128(23):4873–4880.

Schindelin, J., Arganda-Carreras, I., Frise, E., Kaynig, V., Longair, M., Pietzsch, T., Preibisch, S., Rueden, C., Saalfeld, S., Schmid, B., Tinevez, J.-Y., White, D. J., Hartenstein, V., Eliceiri, K., Tomancak, P., and Cardona, A. (2012). Fiji: an open-source platform for biological-image analysis. *Nature Methods*, 9(7):676–682.

Shih, N. P., François, P., Delaune, E. A., and Amacher, S. L. (2015). Dynamics of the slowing segmentation clock reveal alternating two-segment periodicity. *Development*, 142(10):1785–1793.

Shimojo, H., Isomura, A., Ohtsuka, T., Kori, H., Miyachi, H., and Kageyama, R. (2016). Oscillatory control of Delta-like1 in cell interactions regulates dynamic gene expression and tissue morphogenesis. *Genes & Development*, 30(1):102–116.

Sonnen, K. F., Lauschke, V. M., Uraji, J., Falk, H. J., Petersen, Y., Funk, M. C., Beaupeux, M., François, P., Merten, C. A., and Aulehla, A. (2018). Modulation of Phase Shift between Wnt and Notch Signaling Oscillations Controls Mesoderm Segmentation. *Cell*, 172(5):1079–1090.e12.

Soroldoni, D., Jörg, D. J., Morelli, L. G., Richmond, D. L., Schindelin, J., Jülicher, F., and Oates, A. C. (2014). A Doppler effect in embryonic pattern formation. *Science*, 345(6193):222–225.

Sun, X., Meyers, E. N., Lewandoski, M., and Martin, G. R. (1999). Targeted disruption of Fgf8 causes failure of cell migration in the gastrulating mouse embryo. *Genes & Development*, 13(14):1834–1846.

Takada, S., Stark, K. L., Shea, M. J., Vassileva, G., McMahon, J. A., and McMahon, A. P. (1994). Wnt-3a regulates somite and tailbud formation in the mouse embryo. *Genes & Development*, 8(2):174–189.

Takashima, Y., Ohtsuka, T., González, A., Miyachi, H., and Kageyama, R. (2011). Intronic delay is essential for oscillatory expression in the segmentation clock. *Proceedings of the National Academy of Sciences*, 108(8):3300–3305.

Tam, P. P. L. and Loebel, D. A. F. (2007). Gene function in mouse embryogenesis: get set for gastrulation. *Nature Reviews Genetics*, 8(5):368–381.

Torrence, C. and Compo, G. P. (1998). A Practical Guide to Wavelet Analysis. *Bulletin of the American Meteorological Society*, 79(1):61–78.

Tsiairis, C. D. and Aulehla, A. (2016). Self-Organization of Embryonic Genetic Oscillators into Spatiotemporal Wave Patterns. *Cell*, 164(4):656–667.

Udan, R. S., Piazza, V. G., Hsu, C.-W., Hadjantonakis, A.-K., and Dickinson, M. E. (2014). Quantitative imaging of cell dynamics in mouse embryos using light-sheet microscopy. *Development (Cambridge, England)*, 141(22):4406–4414.

Vasiliauskas, D. and Stern, C. D. (2001). Patterning the Embryonic Axis: FGF Signaling and How Vertebrate Embryos Measure Time. *Cell*, 106(2):133–136.

Vibe, C. B. (2020). *The temperature response of the medaka segmentation clock and its link to robustness in embryonic patterning*. PhD thesis, Ruperto-Carola University of Heidelberg.

Yamaguchi, T. P., Harpal, K., Henkemeyer, M., and Rossant, J. (1994). fgfr-1 is required for embryonic growth and mesodermal patterning during mouse gastrulation. *Genes & Development*, 8(24):3032–3044.

Yoshioka-Kobayashi, K., Matsumiya, M., Niino, Y., Isomura, A., Kori, H., Miyawaki, A., and Kageyama, R. (2020). Coupling delay controls synchronized oscillation in the segmentation clock. *Nature*, 580(7801):119–123.

APPENDIX A

Supplementary Movies

Supplementary movies are available at the following links:

`https://github.com/tomitatakehito/Movies_TT_thesis_mov` (.mov format)
`https://github.com/tomitatakehito/Movies_TT_thesis_avi` (.avi format)

Time is indicated in hr:min, and scale bar represents 200 µm in all of the movies.

Movie 1: Line of interest used to generate surface kymographs from LuVeLu signal. *The text for this legend has been originally written by Takehito Tomita and adapted from [Falk et al. (2021)] in revision:* "Related to Fig. 3.2. LuVeLu (cyan) fluorescence in an embryo imaged from the early bud stage is shown from posterior (top) and side orientation (bottom). On the right, the line of interest used to generate a surface kymograph is overlaid."

Movie 2: Transferred line of interest on cell tracking datasets. *The text for this legend has been originally written by Takehito Tomita and adapted from [Falk et al. (2021)] in revision:* "Related to Fig. 3.3. Cell locations in the cell tracking datasets are represented as octahedrons, with color codings as shown in Fig. 3.3A. The transferred line of interest used to generate cell track/flow plots in Fig. 3.3B is represented as a line of white spheres. Cells within 30 µm of the line of interest are colored red. The datasets are aligned in time so that 00:00 is set to the timepoint which corresponds to the start of the first wave."

Movie 3: LuVeLu expression dynamics seen in the mPSM with exogenous FGF8b ligand. Related to Fig. 5.3. Movies showing LuVeLu expression dynamics in the mPSM in either control medium (top) or 8 µg/ml FGF8b medium (bottom).

Movie 4: Dusp4-T2A-3xmVenus expression dynamics seen in the mPSM with exogenous FGF8b ligand, or FGF signaling inhibitor PD0325901. Related to Fig. 5.4. Movies showing Dusp4-T2A-3xmVenus expression dynamics in the mPSM in control, 2 µg/ml, or 8 µg/ml FGF8b medium medium (top row) or 6 µM or 18 µM PD0325901 medium (bottom row).

Movie 5: LuVeLu expression dynamics seen in the mPSM when FGF8b ligand is added ad hoc. Related to Fig. 5.6. Movies showing LuVeLu expression dynamics in the

mPSM in ad hoc addition experiments, where exogenous FGF8b ligand concentration was changed as: 0 ⇒ 0 µg/ml condition (left), 0 ⇒ 4 µg/ml condition (center), 0 ⇒ 8 µg/ml condition (right). The medium switch occurs at 16 hours in imaging.

Movie 6: LuVeLu expression dynamics seen in the mPSM with local administration of FGF8b ligand by beads Related to Fig. 5.7. Movies showing LuVeLu expression dynamics in the mPSM in bead experiments. The bead is shown in cyan hot LUT, while LuVeLu expression is shown in Fire LUT. Control bead condition (top), FGF8b bead condition (bottom).

This thesis was typeset with LaTeX 2_ε, using the istaustriathesis document class developed by Thomas Auzinger. The istaustriathesis document class can be found at `https://gitlab.com/ThomasAUZINGER/istaustriathesis`